Meteoritics & Planetary Science 38, Nr 1, 157–173 (2003)
Abstract available online at http://meteoritics.org

Noble gases and cosmogenic radionuclides in the Gold Basin L4 chondrite shower: Thermal history, exposure history, and pre-atmospheric size

K. C. WELTEN[1]*, M. W. CAFFEE[2†], I. LEYA[3], J. MASARIK[4], K. NISHIIZUMI[1], and R. WIELER[3]

[1]Space Sciences Laboratory, University of California, Berkeley, California 94720–7450, USA
[2]Center for Accelerator Mass Spectrometry, Lawrence Livermore National Laboratory, Livermore, California 94551, USA
[3]ETH Zürich, Isotope Geology and Mineral Resources, NO C61, CH-8092 Zürich, Switzerland
[4]Department of Nuclear Physics, Komensky University, Mlynska dolina F/1, Sk-84215 Bratislava, Slovakia
[†]Present address: Department of Physics, Purdue University, West Lafayette, Indiana 47907, USA
[*]Corresponding author. E-mail: kcwelten@uclink4.berkeley.edu

(Received 18 April 2002; revision accepted 26 September 2002)

Abstract–We measured the concentrations of the cosmogenic radionuclides ^{10}Be, ^{26}Al, ^{36}Cl, and ^{41}Ca in the stone and metal fractions of 15 fragments of the Gold Basin L4 chondrite shower, as well as noble gases in 18 Gold Basin fragments. A comparison of ^{10}Be, ^{26}Al, and ^{41}Ca concentrations with calculated production rates from two different models indicates that the Gold Basin samples came from depths of about 10 cm to more than 150 cm in an object with a radius of 3–5 m. As was predicted by recent model calculations, the noble gases show a reversal of the ^{22}Ne/^{21}Ne ratio at very high shielding. The ^{21}Ne/^{10}Be and ^{21}Ne/^{26}Al ratios in most samples are constant and correspond to a 4π exposure age of 18 ± 2 Myr. However, three Gold Basin samples show a 30–120% excess of ^{21}Ne implying that they were previously exposed close to the surface of the parent body, whereas the other samples were buried several meters deeper. Concentrations of neutron-capture ^{36}Ar in most samples are consistent with measured concentrations of neutron-capture ^{36}Cl and an exposure age of 18 Myr. Large excesses of neutron-capture ^{36}Ar were found in those samples with an excess of ^{21}Ne, providing additional evidence of a first-stage exposure on the parent body. The excess of spallation-produced ^{21}Ne and neutron-capture-produced ^{36}Ar in these samples indicate a first-stage exposure of 35–150 Myr on the parent body. The radiogenic ^{4}He and ^{40}Ar concentrations indicate a major impact on the parent body between 300 and 400 Myr ago, which must have preceded the impacts that brought the Gold Basin meteoroid to the surface of the parent body and then expelled it from the parent body 18 Myr ago.

INTRODUCTION

Gold Basin is a large L4 chondrite shower, discovered recently in the eastern part of the Mojave Desert, Arizona (Kring et al. 2001). The first sample of this shower was identified in 1995 and since then more than 5,000 fragments totaling >185 kg in mass have been recovered from a strewn field with a total area of 225 km^2. Based on ^{10}Be and ^{14}C concentrations in several fragments, the terrestrial age was determined to be 15,000 ± 600 yr and the pre-atmospheric radius of this meteorite was estimated to be 3–4 meters (Kring et al. 2001). Gold Basin is one of the largest finds of chondrites, thus providing a unique opportunity for comparing measured cosmogenic nuclide concentrations with model calculations for large objects. As most samples were found on bedrock and on modern soils, it seems unikely that they were significantly transported after impact. Therefore, one of the initial goals was to establish the possible relationship between the location of samples in the strewn field and the location of samples within the meteoroid.

We measured noble gas concentrations in 18 fragments of the Gold Basin shower. Six of these fragments were analyzed for ^{14}C and/or ^{10}Be earlier (Kring et al. 2001). Thirteen of the fragments analyzed for noble gases and two additional samples selected by D. Kring were also analysed for cosmogenic radionuclides. We measured concentrations of ^{10}Be (half-life = 1.5 × 10^6 yr), ^{26}Al (7.05 × 10^5 yr), ^{36}Cl (3.01 × 10^5 yr), and ^{41}Ca (1.04 × 10^5 yr) in both stone and metal fractions in order to constrain the pre-atmospheric radius of the Gold Basin meteorite and determine the depth of each sample within the meteoroid. Measured concentrations of ^{10}Be, ^{26}Al, and neutron-capture-produced ^{41}Ca were compared on calculations based on the Los Alamos High Energy Transport (LAHET) Code System (Reedy and

Table 1. Elemental concentrations in metal (m) and stone (s) fraction of Gold Basin samples. All concentrations are in wt%. Fraction of oxidized metal in stone fraction, $f(M_{OX}) = (Fe_{ST} + Ni_{ST} - 16.1)/(65.0 - 16.1)$.

Sample	Mg(m)	Fe(m)	Ni(m)	Mg(s)	Al(s)	K(s)	Ca(s)	Fe(s)	Ni(s)	$f(M_{OX})$
UA-1217	–	–	–	16.3	1.24	0.086	1.79	16.4	0.35	0.014
UA-682	0.019	86.3	14.2	12.8	1.36	0.111[a]	1.39	21.4	0.72	0.123
UA-263	0.028	84.2	17.2	14.1	1.21	0.081	1.26	16.8	0.37	0.022
UA-1164	0.074	88.6	12.3	14.0	1.20	0.093[a]	1.33	19.1	0.45	0.070
LPL-1012	0.032	86.9	14.7	13.5	1.23	0.111[a]	1.46	20.1	0.51	0.092
UA-285	0.029	85.6	14.4	14.8	1.32	0.082	1.55	17.0	0.21	0.023
UA-274	–	–	–	16.4	1.29	0.075	1.92	17.9	0.56	0.047
UA-418	0.038	87.2	12.5	13.4	1.20	0.086	1.48	18.0	0.58	0.051
UA-426	0.015	85.5	15.6	15.1	1.25	0.078	1.55	17.7	0.41	0.041
ZH-3	0.108	80.4	14.3	15.3	1.18	0.092[a]	1.48	18.6	0.80	0.067
LPL-1011	0.033	82.5	16.4	14.3	1.14	0.080	1.60	17.1	0.17	0.024
UA-300	–	–	–	15.1	1.19	0.080	1.68	19.3	0.47	0.075
UA-639	0.019	86.3	15.6	14.8	1.26	0.070	1.41	18.2	0.38	0.050
UA-1188	0.018	82.2	17.0	13.4	1.23	0.102[a]	1.33	18.5	0.45	0.059
ZH-2	0.081	81.5	13.1	15.7	1.31	0.105	1.68	17.0	0.59	0.031

[a]K contents >0.09% are probably due to terrestrial contamination, since they seem correlated with the weathering grade of a meteorite, as judged from the high Fe and Ni concentrations in the stone fraction of these samples.

Masarik 1994) and to a semi-empirical model (Nagai et al. 1993; Honda et al. 2002).

In this work, we also examine the exposure history of the Gold Basin meteoroid using the $^{10}Be/^{21}Ne$ and $^{26}Al/^{21}Ne$ methods (Graf, Baur, and Signer 1990a). In addition, we compare the neutron-capture-produced ^{36}Cl and ^{36}Ar concentrations to explore the possibility that some fragments were exposed under considerable shielding on the parent body.

EXPERIMENTAL PROCEDURES

Radionuclide and Elemental Analyses

Samples consisting of 2–3 g of material were gently crushed in an agate mortar and metal was separated with a magnet. The metal was cleaned several times in a ultrasonic bath with 0.2N HCl and once or twice with concentrated HF to remove attached troilite and silicates. After adding carrier solutions containing 0.8–2.0 mg of Be, Al, Ca, and 2–5 mg of Cl, metal samples of 20–130 mg were dissolved in 1.5N HNO_3. The non-magnetic fraction (mainly silicates) was homogenized and samples of ~100 mg were dissolved with ~3 mg of Be and Cl carriers in a mixture of concentrated HF/HNO_3. After dissolution, aliquots were taken for chemical analysis by atomic absorption spectroscopy (AAS). For the metal samples, we measured the major elements Fe and Ni as well as the concentration of Mg in order to estimate the amount of silicate contamination. For the silicate samples, we measured the concentrations of Mg, Al, K, Ca, Fe, and Ni. The last four are the major target elements for the production of ^{36}Cl, whereas concentrations of Fe and Ni provide an estimate of the amount of oxidized metal in the stone fraction (Welten et al. 2001b). The results of these measurements are given in Table 1.

After dissolution, Cl was precipitated as AgCl and Be, Al, and Ca were separated by ion exchange chromatography techniques and acetyl-acetone extraction. All radionuclide concentrations were measured by accelerator mass spectrometry (AMS) at the Lawrence Livermore National Laboratory (Davis et al. 1990). Measured $^{10}Be/Be$, $^{26}Al/Al$, $^{36}Cl/Cl$, and $^{41}Ca/Ca$ ratios were corrected for isobaric interferences and chemical blanks and normalized to ^{10}Be, ^{26}Al, ^{36}Cl, and ^{41}Ca standards prepared by one of the authors (K. Nishiizumi) as described previously (Nishiizumi et al. 1984; Sharma et al. 1990; Nishiizumi, Caffee, and DePaolo 2000). These results are shown in Table 2 and include all known AMS uncertainties (1σ) of the samples, standards, and blanks, but not the uncertainties in the absolute values of the AMS standards.

Noble Gas Analyses

A total of 32 samples from 18 different Gold Basin fragments were analyzed. Samples consisted of one or several chips (120–250 mg) of meteorite, free of fusion crust, wrapped in aluminum foil. Prior to analysis, samples were preheated for about a day at ~130 ºC to desorb loosely bound atmospheric noble gases. Helium, neon, and argon were measured as described by Wieler et al. (1989). For most Gold Basin fragments, two or three samples were measured. Results for each sample are given in Table A1 (appendix), whereas Table 3 gives adopted values for each fragment, which are the average values if two or more measurements were done.

Duplicate analyses on small chips of the same fragment generally give reproducible He and Ne concentrations, whereas the Ar concentrations show considerably more scatter (Table A1). For three samples (UA-274, 418, and 1164), one aliquot also shows significantly lower ^{3}He (20–30%) and ^{21}Ne

Table 2. Concentrations of cosmogenic radionuclides in metal and stone fraction and/or bulk (b) samples of Gold Basin L4 chondrite shower. All radionuclide concentrations are given in dpm/kg; quoted errors include all known uncertainties in the AMS measurements, but not those of the absolute isotopic ratios of the AMS standards. Measured concentrations of ^{10}Be and ^{26}Al in the metal fraction (in parentheses) were corrected for silicate contamination (see text).

Sample[a]	^{10}Be(s)	^{10}Be(m)	^{10}Be(b)[b]	^{26}Al(s)	^{26}Al(m)	^{36}Cl(s)	^{36}Cl(m)	^{41}Ca(s)	^{41}Ca(m)
UA-1217	15.5 ± 0.3	–	12.2 ± 0.3	49.2 ± 1.0	–	9.7 ± 0.2	–	10.3 ± 0.5	–
UA-682	12.7 ± 0.2	2.53 ± 0.07 (2.54)	–	41.0 ± 1.0	1.77 ± 0.07 (1.81)	10.2 ± 0.2	12.3 ± 0.25	8.7 ± 0.5	16.0 ± 1.9
UA-263	9.9 ± 0.2	1.53 ± 0.04 (1.54)	8.4 ± 0.4	32.9 ± 0.9	1.21 ± 0.04 (1.26)	10.4 ± 0.5	8.45 ± 0.17	7.2 ± 0.4	10.2 ± 0.5
UA-1164	10.3 ± 0.2	1.68 ± 0.04 (1.72)	8.3 ± 0.4	31.2 ± 0.8	1.10 ± 0.05 (1.23)	10.9 ± 0.3	7.77 ± 0.16	10.4 ± 0.5	9.1 ± 0.5
LPL-1012	8.30 ± 0.16	1.09 ± 0.02 (1.10)	–	28.2 ± 0.7	0.80 ± 0.03 (0.85)	14.0 ± 0.3	5.94 ± 0.12	13.0 ± 0.6	7.4 ± 0.4
UA-285	7.02 ± 0.14	0.82 ± 0.02 (0.83)	–	23.7 ± 0.6	0.58 ± 0.02 (0.62)	12.9 ± 0.3	4.23 ± 0.08	14.5 ± 1.0	4.5 ± 0.2
UA-274	5.96 ± 0.12	–	4.2 ± 0.1	20.1 ± 0.4	–	13.6 ± 0.3	–	17.3 ± 0.6	–
UA-418	5.19 ± 0.10	0.65 ± 0.01 (0.66)	–	17.1 ± 0.4	0.46 ± 0.02 (0.49)	8.0 ± 0.2	3.26 ± 0.07	10.2 ± 0.6	3.5 ± 0.2
UA-426	3.67 ± 0.07	0.40 ± 0.01 (0.40)	–	12.7 ± 0.3	0.29 ± 0.02 (0.31)	6.6 ± 0.1	2.06 ± 0.04	9.1 ± 0.6	3.0 ± 0.2
ZH-3	3.07 ± 0.06	0.29 ± 0.01 (0.31)	–	11.2 ± 0.2	0.20 ± 0.01 (0.27)	5.9 ± 0.1	1.79 ± 0.04	8.7 ± 0.4	1.8 ± 0.2
UA-300	2.16 ± 0.04	–	1.74 ± 0.08	7.1 ± 0.2	–	7.5 ± 0.2	–	6.7 ± 0.3	–
LPL-1011	2.30 ± 0.05	0.20 ± 0.01 (0.20)	–	6.9 ± 0.2	0.14 ± 0.01 (0.15)	3.7 ± 0.1	1.01 ± 0.02	5.1 ± 0.3	–
UA-639	1.88 ± 0.04	0.18 ± 0.01 (0.18)	–	6.5 ± 0.2	0.12 ± 0.01 (0.12)	5.4 ± 0.1	1.02 ± 0.03	5.3 ± 0.4	–
UA-1188	1.21 ± 0.02	0.13 ± 0.03 (0.13)	1.33 ± 0.04	4.2 ± 0.1	0.09 ± 0.01 (0.09)	2.4 ± 0.1	0.72 ± 0.04	2.8 ± 0.3	–
ZH-2	0.98 ± 0.02	0.077 ± 0.002 (0.081)	–	3.3 ± 0.1	0.052 ± 0.006 (0.067)	–	0.48 ± 0.01	–	–

[a]UA- and LPL- samples were obtained from D. Kring, University of Arizona, Tucson; ZH- samples were obtained from a private collector.
[b]Concentrations of ^{10}Be in the bulk are from Kring et al. (2001).

Table 3. Average noble gas concentrations in eighteen Gold Basin L4 chondrite samples. N is the number of duplicate samples measured. All noble gas concentrations are in 10^{-8} cm^3 STP/g. Uncertainties in absolute concentrations are 5%. Uncertainties in Ne istopic ratios and in the ^{36}Ar/^{38}Ar ratio are ~1%.

Sample	N	^{3}He	^{4}He	^{20}Ne	^{21}Ne	^{22}Ne	$(^{22}Ne/^{21}Ne)_c$	$(^3He/^{21}Ne)_c$	^{36}Ar	^{38}Ar	^{40}Ar	$^{38}Ar_{cos}$	^{21}Ne/^{38}Ar
UA-1217	2	17.3	208	4.00	4.39	4.77	1.085	3.95	1.03	0.56	173	0.42	10.5
UA-682	3	29.8	282	7.21	7.98	8.57	1.073	3.73	1.86	0.90	215	0.63	12.7
UA-263	3	15.0	205	4.04	4.50	4.82	1.069	3.33	2.20	0.72	216	0.35	12.0
UA-1164	2	8.82	155	2.39	2.61	2.78	1.062	3.38	0.90	0.38	174	0.24	10.8
ZH-1	1	6.56	133	2.01	2.25	2.41	1.072	2.92	0.86	0.28	151	0.13	17.3
UA-285	2	7.01	157	1.89	2.10	2.25	1.071	3.33	0.93	0.32	221	0.164	12.8
ZH-5	1	4.86	128	1.53	1.70	1.82	1.071	2.86	0.53	0.22	121	0.134	12.7
UA-274	2	5.04	117	1.47	1.62	1.73	1.069	3.12	1.10	0.32	278	0.125	13.0
UA-418	2	4.43	113	1.48	1.48	1.60	1.071	3.00	1.12	0.32	358	0.124	11.9
UA-1221	2	3.53	122	1.06	1.14	1.23	1.071	3.09	0.80	0.23	223	0.087	13.1
UA-426	1	3.00	105	0.91	0.98	1.06	1.077	3.04	0.71	0.23	203	0.106	9.2
ZH-3	1	2.10	110	0.83	0.90	0.97	1.079	2.33	0.53	0.13	175	0.030	30.1
UA-300	2	2.51	137	0.83	0.86	0.94	1.082	2.92	0.60	0.17	270	0.061	14.1
UA-639	2	1.49	118	0.50	0.51	0.56	1.079	2.92	0.72	0.15	162	0.012	42.5
UA-1187	2	1.42	120	0.46	0.48	0.52	1.077	2.98	0.80	0.18	197	0.030	16.0
UA-1188	2	1.09	104	0.38	0.39	0.42	1.076	2.78	0.94	0.23	238	0.055	7.1
ZH-4	1	0.79	93	0.33	0.30	0.33	1.083	2.63	0.38	0.08	175	0.011	27.3
ZH-2	1	0.79	99	0.24	0.28	0.30	1.084	2.82	0.30	0.07	156	0.009	30.8

(10–15%) concentrations than their respective duplicate samples. We conclude that these three samples may have been too close to the fusion crust, resulting in diffusive losses of He and Ne. Therefore, the He and Ne concentrations of these three samples were excluded from the average, whereas we assume that the loss of cosmogenic Ar was less than 10%. The scatter in the Ar results is mainly due to different amounts of adsorbed atmospheric Ar in each sample, as a result of different temperatures and durations of preheating. At least six samples have much higher concentrations of atmospheric Ar than their duplicate samples measured in other runs. For these samples (UA-300, 639, 682, 1164, 1187, and 1188), we excluded the analyses with high atmospheric Ar from the average. In addition, small variations in cosmogenic Ar may arise from variations in concentrations in the main target elements (K, Ca, and Fe). The compositions of the samples analyzed for noble gases are not exactly known, but typical variations in the ^{38}Ar production rate can be estimated from the measured K, Ca, and Fe concentrations in the stone fraction. We conclude that variations in Ca (and other target elements) will not generally result in deviations of more than 10% from the average ^{38}Ar production rate.

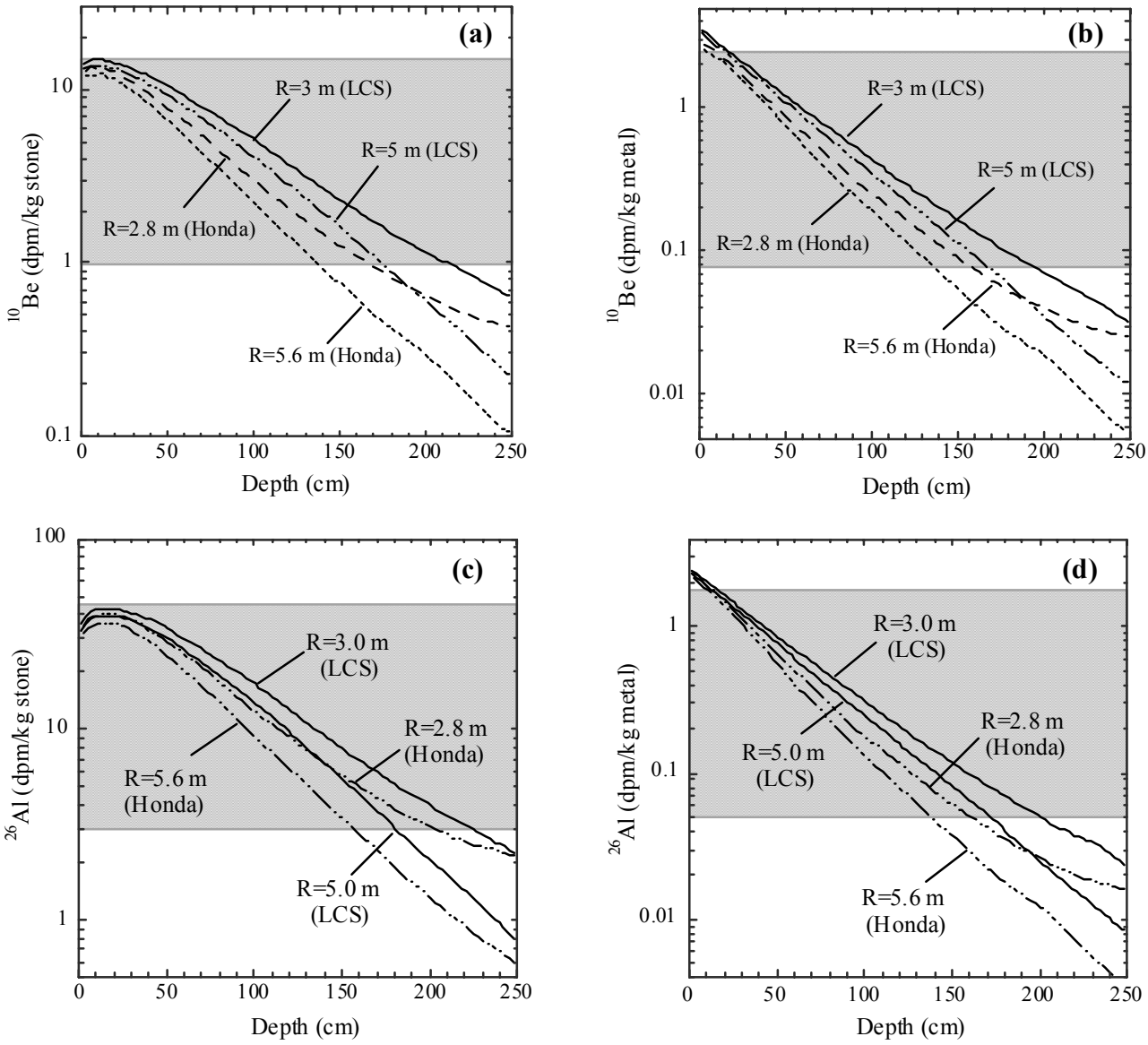

Fig. 1. Calculated depth profiles of ^{10}Be and ^{26}Al production rates in the metal and stone fraction of L chondritic objects with radii of 2.8–5.6 m. Production rates based on the LCS model of Masarik and Reedy (1994), are compared to those based on the Honda model (Nagai et al. 1993; Honda et al. 2002). For the LCS model, we show production rates in objects with radii of 3 and 5 m, whereas for the Honda model, only calculations for 2.8 and 5.6 meters are available. Although the two models show similar ^{10}Be and ^{26}Al production rates in the top 50 cm, differences increase up to a factor of ~2 near the center of large objects.

For the partitioning of the noble gas concentrations into a cosmogenic (c), a radiogenic (r), and a trapped (tr) component, the following assumptions were made: $^{3}He_c = {}^{3}He$, $(^{4}He/^{3}He)_c = 6$, $(^{20}Ne/^{22}Ne)_c = 0.83$, $(^{20}Ne/^{22}Ne)_{tr} = 9.8$, $(^{21}Ne/^{22}Ne)_{tr} = 0.033$, $(^{36}Ar/^{38}Ar)_c = 0.65$ and $(^{36}Ar/^{38}Ar)_{tr} = 5.32$. Trapped Ne corrections were always less than 1.5% for ^{22}Ne and less than 0.1% for ^{21}Ne. Trapped Ar corrections were much higher, up to ~90% for ^{38}Ar, but the trapped Ar component may have been overestimated for samples containing significant concentrations of neutron-capture ^{36}Ar, as will be discussed later.

Model Calculations

To calculate the fluxes of primary and secondary particles in L chondrites with radii of 1, 2, 3, and 5 m and for 2π irradiation, we used the LAHET Code System (LCS) (Masarik and Reedy 1994a; Masarik, Nishiizumi, and Reedy 2001). The LCS model combines the LAHET code (Prael and Lichtenstein 1989) for interactions of charged particles and neutrons above 20 MeV and the Monte Carlo N-Particle (MCNP) code (Briesmeister 1993) for low-energy neutrons. For meteoroid orbits, the LCS model uses an effective flux of

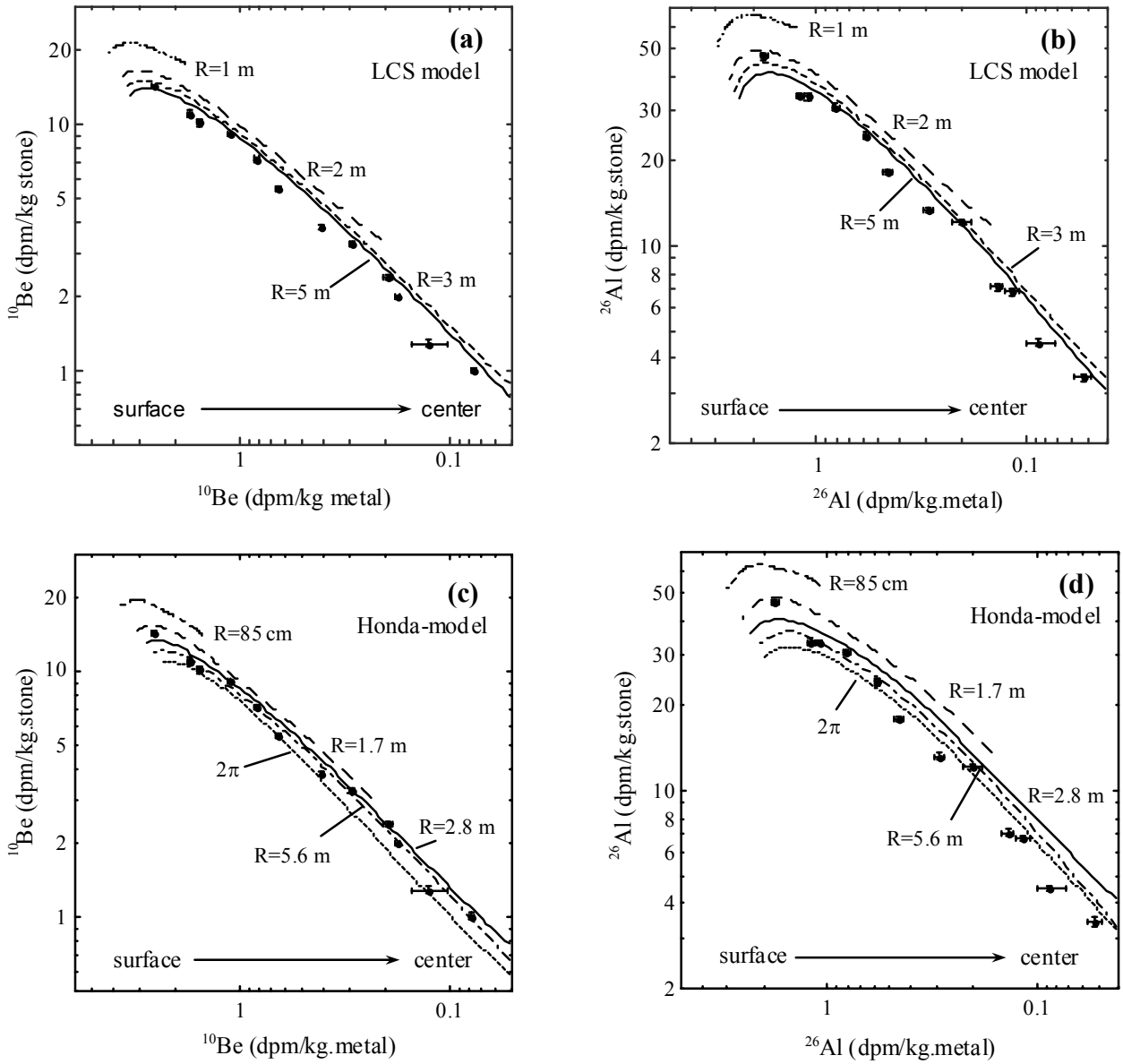

Fig. 2. Measured concentrations of ^{10}Be and ^{26}Al in the metal and stone fraction of Gold Basin samples are compared with calculated production rates based on the LCS model (Fig. 2a–b) and on Honda's semi-empirical model (Fig. 2c–d) for L chondrites with radii of 85 cm–5.6 m. Although none of the calculated profiles exactly match the experimental data, they indicate that the Gold Basin meteoroid most likely had a radius between 200 and 500 cm. Note that the ^{10}Be and ^{26}Al concentrations on the x-axis decrease from left to right, corresponding to increasing shielding depth.

primary GCR particles of 4.8 nucleons cm^{-2} s^{-1} for energies above 10 MeV. This flux was ascertained from radionuclide concentrations in Knyahinya (Reedy et al. 1993). For proton-induced reactions, we used experimental cross sections (e.g. Dittrich et al. 1990). Very little experimental data are available for neutron-induced reactions (e.g. Imamura et al. 1990). Therefore, neutron cross sections were adjusted (from the proton cross sections) to match the calculated production rates with measured concentrations in the metal and stone phase of the Knyahinya chondrite (Reedy et al. 1993), in the ellipsoidal St. Severin chondrite (Masarik and Reedy 1994b), in the Canyon Diablo iron meteorite (Michlovich et al. 1994), and in the lunar surface (Reedy and Masarik 1994; Masarik, Nishiizumi, and Reedy 2001).

Using the calculated fluxes of primary and secondary particles and experimental proton and adjusted neutron cross sections, we calculated the production rates of ^{10}Be, ^{26}Al, and ^{21}Ne by spallation reactions. The production rate of ^{26}Al in the metal fraction was derived from the calculated production rate of ^{10}Be in the metal by simply adopting a constant ^{26}Al/^{10}Be production rate of 0.7 (Lavielle et al. 1999; Albrecht et al. 2000). The latter ratio corresponds better with

Table 4. Parameters used for the estimation of production of ^{10}Be, ^{26}Al in stone (s) and metal (m) fractions of chondritic objects, and of neutron-capture ^{41}Ca from Ca.

Nuclide	ΔA'	*f*
^{10}Be(m)	28	0.18
^{26}Al(m)	34	0.23
^{10}Be(s)	11	0.11
^{26}Al(s)	7	0.11
^{41}Ca(Ca)	1.5	0.065

experimental values than calculated ratios, which decrease from a value of ~0.56 at the surface of large objects to <0.4 in the center of a 3 m object.

In addition, we calculated depth profiles using the semi-empirical model of Honda (1988), which is explored in more detail by Nagai et al. (1993) and Honda et al. (2002). This model, which we will refer to as the Honda-model, uses two universal shielding parameters as a function of size and depth in chondritic meteorites. One parameter (k'_2) is a measure of the irradiation hardness of the flux, the other one (k'_1) of the intensity of the irradiation. Values for these two parameters are given as a function of size and depth for chondritic objects (Nagai et al. 1993, Table 3, Appendix). Using these parameters, the production rate, P, of a certain nuclide, X, is given as: $P(X) = f^* k'_1 *(\Delta A')^{-k'2}$, in which *f* is the partial isobaric yield and ΔA' the effective mass difference between product and target nuclei. Table 4 lists the used values of *f* and ΔA' for the production of ^{10}Be and ^{26}Al in the metal and stone fraction of chondrites as well as for the production of neutron-capture ^{41}Ca from Ca (Nagai et al. 1993; Honda et al. 2002). The advantage of this model is that it is based on meteoroids with a wide range in size, including objects with radii of several meters, such as the Tsarev L5 chondrite (Nagai et al. 1993) and the Brenham pallasite (Honda et al. 2002).

RESULTS AND DISCUSSION

Elemental Concentrations

Measured concentrations of Mg in the dissolved metal samples correspond to silicate contaminations of less than 0.2 wt% for most samples, except for UA-1164 (0.4 wt%), ZH-2 (0.5 wt%), and ZH-3 (0.6 wt%). The measured concentrations of Fe (16.4–21.4 wt%) and Ni (0.17–0.80 wt%) in the stone fraction (Table 2) are significantly higher than the average literature values of 16.0 ± 0.6 wt% Fe (Jarosewich 1990) and 0.05 ± 0.02 wt% Ni for L chondrite falls (Rambaldi, Cendales, and Thacker 1978). Based on equations given in Welten (1999), we calculate that the stone fraction of the Gold Basin samples contains between 1.4 wt% (UA-1217) and 12.3 wt% (UA-682) of oxidized metal (Table 1), which is here defined as a mixture of hydrated Fe and Ni oxides. These values cannot directly be compared with the Mössbauer results of Kring et al. (2001), but confirm their observation

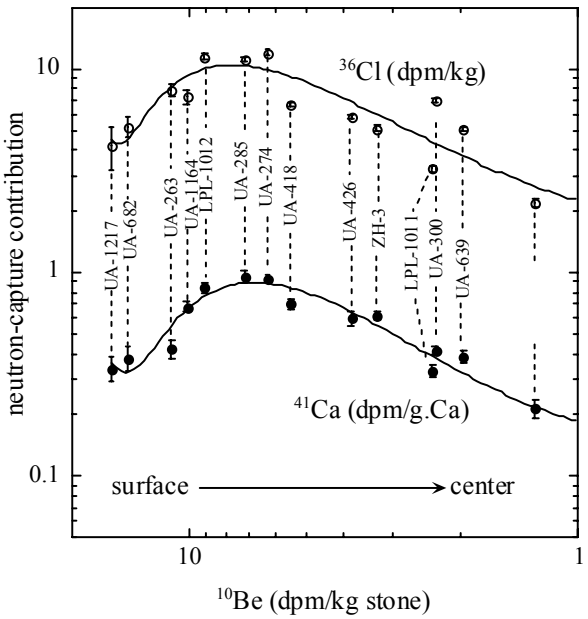

Fig. 3. Neutron-capture ^{36}Cl and ^{41}Ca in the stone fraction as a function of the ^{10}Be concentration, which decreases (from left to right) with increasing shielding. The neutron-capture concentrations of ^{36}Cl and ^{41}Ca are obtained by subtracting spallation-produced ^{36}Cl and ^{41}Ca from the measured concentrations in the stone fraction. The neutron-capture ^{41}Ca contribution is normalized to the amount of Ca in each sample (dpm/g.Ca). The dashed and solid lines represent the best fits through the ^{36}Cl and ^{41}Ca data.

that there is considerable variation in the degree of oxidation from sample to sample. These observed differences in weathering are probably due to 1) differences in burial conditions, i.e., some of the samples were found on the surface, whereas others were found up to 25 cm deep, and 2) drainage conditions, i.e., some samples were found on desert pavement while others were found on mountain slopes or in drainage systems.

The high degree of weathering of some of the Gold Basin samples also implies that the concentrations of ^{10}Be and ^{26}Al in the stone fraction were significantly diluted by oxidized metal. The concentrations of Mg, Al, and Ca in the stone fraction show a slight decrease with increasing amount of oxidized metal (Table 1), as would be expected on the basis of a simple dilution effect of the stone fraction (containing Mg, Al, Ca) with oxidized metal. The observation that none of the samples shows anomalously low lithophile concentrations indicates that none of the Gold Basin samples was weathered as severely as some of the Roosevelt County meteorites, from which considerable amounts of Mg, Si, and Ca were leached (Bland et al. 1998).

Radionuclide Results

Measured concentrations of ^{10}Be, ^{26}Al, ^{36}Cl, and ^{41}Ca in

Table 5. Spallation (sp) and neutron-capture (nc) component of ^{36}Cl and ^{41}Ca component in stone fraction as well as estimated and calculated neutron-capture component of ^{36}Ar in bulk of Gold Basin samples.

Sample	$^{10}Be_s/^{10}Be_m$	$^{a}P(^{36}Cl)_{Ca}/P(^{36}Cl)_{Fe}$	^{36}Cl(sp) dpm/kg	^{36}Cl(nc) dpm/kg	^{41}Ca(sp) dpm/kg	^{41}Ca(nc) dpm/kg	^{41}Ca(nc)^{b} dpm/gCa	^{36}Ar(cap) est.^{c}	^{36}Ar(cap) calc.^{d}
UA-1217	5.0 ± 0.5	–	5.6 ± 0.6	4.2 ± 0.6	4.8 ± 0.6	5.5 ± 0.7	0.34 ± 0.05	0.40 ± 0.20	0.15 ± 0.04
UA-682	5.5 ± 0.2	13.3 ± 1.3	5.2 ± 0.4	5.2 ± 0.5	3.9 ± 0.5	4.8 ± 0.7	0.38 ± 0.05	1.19 ± 0.25	0.18 ± 0.03
UA-263	6.8 ± 0.3	15.7 ± 1.6	3.3 ± 0.3	7.3 ± 0.6	2.4 ± 0.1	4.8 ± 0.4	0.42 ± 0.04	1.00 ± 0.50	0.25 ± 0.04
UA-1164	6.5 ± 0.3	15.2 ± 1.5	3.3 ± 0.2	7.9 ± 0.4	2.18 ± 0.13	8.2 ± 0.5	0.68 ± 0.04	0.42 ± 0.19	0.27 ± 0.05
LPL-1012	8.4 ± 0.3	18.2 ± 1.8	3.0 ± 0.2	11.5 ± 0.4	1.83 ± 0.10	11.2 ± 0.6	0.84 ± 0.05	–	0.39 ± 0.05
UA-285	8.8 ± 0.3	18.8 ± 1.9	2.08 ± 0.16	11.2 ± 0.4	1.15 ± 0.06	13.4 ± 1.0	0.95 ± 0.07	0.46 ± 0.16	0.39 ± 0.05
UA-274	9 ± 1	19 ± 2	2.03 ± 0.15	12.0 ± 0.4	1.10 ± 0.14	16.2 ± 0.7	0.93 ± 0.04	0.36 ± 0.12	0.41 ± 0.05
UA-418	8.4 ± 0.3	18.3 ± 1.8	1.57 ± 0.12	6.7 ± 0.2	0.87 ± 0.06	9.3 ± 0.6	0.70 ± 0.05	0.28 ± 0.11	0.23 ± 0.03
UA-426	9.5 ± 0.3	19.7 ± 2.0	1.06 ± 0.08	5.8 ± 0.2	0.75 ± 0.05	8.3 ± 0.6	0.59 ± 0.04	0.07 ± 0.07	0.20 ± 0.03
ZH-3	11.1 ± 0.3	21.6 ± 2.2	0.95 ± 0.07	5.1 ± 0.2	0.44 ± 0.05	8.2 ± 0.4	0.62 ± 0.03	0.36 ± 0.07	0.18 ± 0.03
UA-300	11 ± 1	21 ± 2	0.71 ± 0.05	7.1 ± 0.2	0.37 ± 0.05	6.3 ± 0.3	0.42 ± 0.02	0.34 ± 0.14	0.25 ± 0.05
LPL-1011	12.4 ± 0.7	23.0 ± 2.3	0.58 ± 0.05	3.2 ± 0.1	0.32 ± 0.02	4.8 ± 0.3	0.33 ± 0.02	–	0.11 ± 0.02
UA-639	11.1 ± 0.3	21.6 ± 2.2	0.53 ± 0.04	5.1 ± 0.1	0.29 ± 0.03	5.0 ± 0.4	0.39 ± 0.03	0.21 ± 0.04	0.17 ± 0.03
UA-1188	10.3 ± 2.1	21 ± 3	0.35 ± 0.03	2.2 ± 0.1	0.20 ± 0.02	2.6 ± 0.3	0.22 ± 0.02	0.04 ± 0.03	0.07 ± 0.01
ZH-2	12.7 ± 0.5	23.2 ± 2.3	0.29 ± 0.02	–	0.13 ± 0.03	–	–	0.12 ± 0.02	–

[a]Calculated using $P(^{36}Cl)_{Ca}/P(^{36}Cl)_{Fe} = 27.6*\log(^{10}Be_s/^{10}Be_m) - 7.3$ (Welten et al. 2001b).

[b]Corrected for radioactive decay during the terrestrial residence time of 15 kyr.

[c]The neutron-capture component (in 10^{-8} cm^3 STP/g) is estimated using a cosmogenic ^{21}Ne/^{38}Ar ratio of 8 ± 1 and ^{36}Ar/^{38}Ar ratios of 0.65 for the cosmogenic and 5.32 for the trapped Ar component; only for UA-682 and UA-1217, we assumed a cosmogenic ^{21}Ne/^{38}Ar ratio of 9 ± 1 in order to prevent negative values for the trapped ^{36}Ar component.

[d]Calculated on the basis of neutron-capture ^{36}Cl (dpm/kg) and a single-stage (4π) exposure of 18 ± 2 Myr.

the stone fraction (s), as well as the metal fraction (m), are given in Table 2. The measured ^{10}Be and ^{26}Al concentrations in the metal fraction were corrected for small contributions of ^{10}Be and ^{26}Al from silicate contamination. Silicate corrections were typically <2% for ^{10}Be, whereas corrections for ^{26}Al ranged from 3–10%. Except for UA-1188, our ^{10}Be concentrations measured in the stone fraction are ~25% higher on average than those measured by Kring et al. (2001) in bulk samples. The lower values in bulk samples are partly due to the presence of metal, but even after correction for the amount of metal separated, our values are still ~20% higher. The lower values of Kring et al. (2001) are most likely due to a systematic difference between our ^{10}Be standard and the one used by Kring et al. (2001).

The concentrations of ^{10}Be, ^{26}Al, and ^{36}Cl in the metal fraction show variations of a factor of 20–30, decreasing from UA-682 to ZH-2. Since ^{10}Be, ^{26}Al, and ^{36}Cl in the metal fraction are high-energy products, their concentrations systematically decrease with depth. Therefore, UA-682 is the least shielded sample (close to the surface), and ZH-2 is the most shielded sample (close to the center).

The concentrations of ^{10}Be and ^{26}Al in the stone fraction decrease about a factor of 12–15 from the least shielded samples (UA-1217, UA-682) to the most shielded sample (ZH-2). The ^{26}Al/^{10}Be ratio in the stone fraction is relatively constant at 3.3 ± 0.2. This value is comparable to ratios of 3.42 ± 0.18 and 3.5 ± 0.3 found in two other large chondrites, Chico (L6) and Ghubara (L5), respectively (Garrison et al. 1992, Ferko et al. 2002), whereas small and medium-sized meteorites usually show ^{26}Al/^{10}Be ratios ≤3 (Bhandari et al. 1993).

To compare the measured ^{10}Be and ^{26}Al concentrations in the stone fraction with calculated production rates, we have to make corrections for weathering due to the dilution of the stone fraction with oxidized metal. Compared to the stone fraction, concentrations in the metal fraction are 5–12 times lower for ^{10}Be and 25–60 times lower for ^{26}Al. Weathering corrections were determined on the basis of the amount of oxidized metal (Table 1) and the concentrations of ^{10}Be and ^{26}Al in stone and metal fractions. Corrections range from 1–2% for the least weathered samples (UA-263, 1217) to ~10% for the most weathered sample (UA-682). Corrections for radioactive decay during the terrestrial residence time of 15 kyr (Kring et al. 2001) are 0.7% for ^{10}Be, 1.5% for ^{26}Al, 3.5% for ^{36}Cl, and 10% for ^{41}Ca.

Model Calculations

Before we compare the measured radionuclide concentrations with calculated production rates, we must emphasize that the latter are quite model dependent and that differences between the models increase with increasing size and depth. For the medium-sized Knyahinya chondrite, the models give production rates within ~10% of the measured values (Reedy et al. 1993; Nagai et al. 1993; Leya et al. 2000). However, for a chondritic object with a 1 m radius, calculated ^{10}Be production rates from Leya et al. (2000) are 10–20% lower, whereas those from Nagai et al. (1993) are 10–30% lower than in the LCS model. And the differences are somewhat larger for the metal fraction. Because the model of Leya et al. (2000, 2001) only gives production rates for

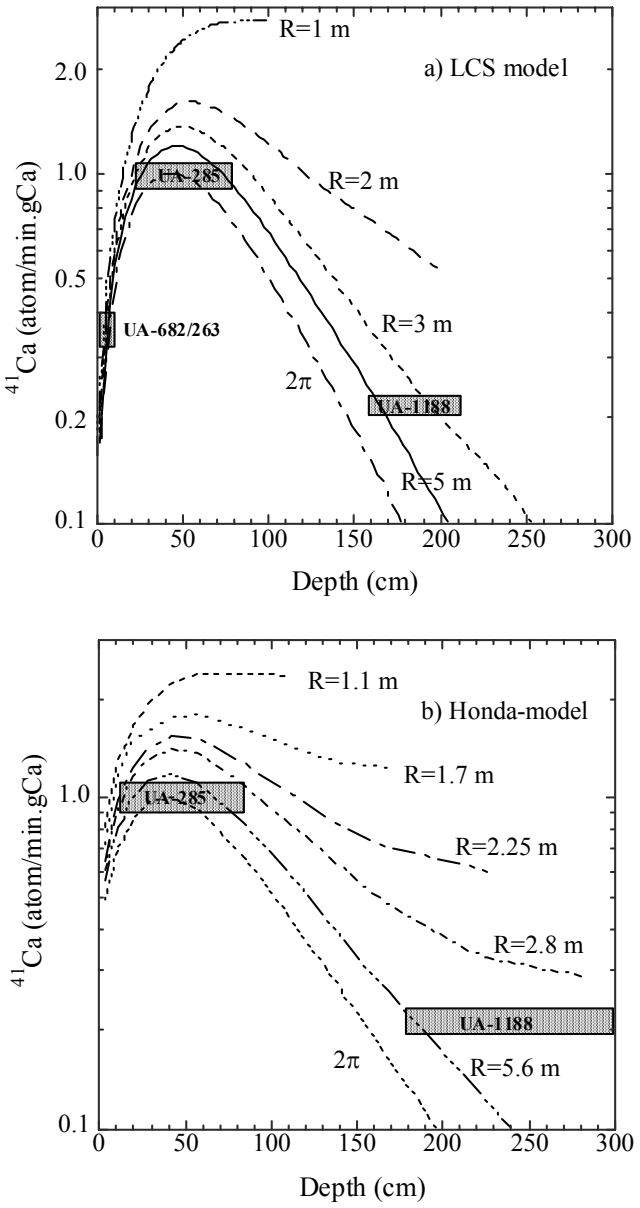

Fig. 4. Depth profiles of neutron-capture ^{41}Ca in L chondrites with radii between 1 and 5 m, as well as for 2π irradiation, calculated by the LCS model (a) and by the semi-empirical model of Honda (b). The peak value of ~1.0 dpm/g.Ca in UA-285 and the lowest values of ~0.2 dpm/g.Ca in UA-1188 indicate a radius larger than 3 m. Assuming a radius of 3–5 m, the most shielded sample was from a depth of at least 150 cm, whereas UA-682 was less than 10 cm from the pre-atmospheric surface.

objects with radii up to 120 cm and for 2π exposure geometries, a direct comparison of the two purely physical models for very large meteoroids is not possible. In Fig. 1, we show calculated ^{10}Be and ^{26}Al production rates in the stone and metal fraction using the LCS model and the Honda model for objects with radii of 2.8–5.6 m. Again, for low shielding conditions (depth <50 cm), the models show relatively good agreement, but at a depth of 250 cm in a 5.0–5.6 m object, the production rates in metal and stone fractions differ by as much as a factor of 2.

Since LCS-based production rates of ^{10}Be and ^{26}Al for 2π exposure conditions are in good agreement with observed depth profiles in the lunar surface up to depths of ~400 g/cm^2 (Reedy and Masarik 1994), we do not expect large systematic errors for LCS-based production rates of ^{10}Be and ^{26}Al in the silicate fraction. However, ^{10}Be and ^{26}Al production rates in the metal fraction are more uncertain, especially for high shielding conditions. This is mainly due to uncertainties in the neutron cross-sections for the Fe(n,x)^{10}Be and Fe(n,x)^{26}Al reactions, which were adjusted from proton cross-sections to fit measured ^{10}Be and ^{26}Al concentrations in the Canyon Diablo iron meteorite (Michlovich et al. 1994). In fact, it was recently pointed out that Canyon Diablo may not be an ideal meteorite to test model calculations (Merchel et al. 2001), in particular because: 1) due to the complex exposure history of Canyon Diablo (Heymann et al. 1966), the ^{3}He/^{21}Ne and ^{4}He/^{21}Ne ratios are not the most reliable depth indicators, and 2) production rates of ^{10}Be and especially ^{26}Al are very sensitive to the inhomogeneous distribution of trace elements such as phosphorus and sulfur, as was recently shown by Leya and Michel (1998). The measured concentrations of ^{10}Be and ^{26}Al in the metal phase of Gold Basin samples may therefore provide additional constraints for the model.

Pre-Atmospheric Size

The saturation values of ^{10}Be and ^{26}Al in the metal and stone fraction are plotted versus calculated production rates from the LCS model (Figs. 2a, b) as well as those derived from the Honda-model (Figs. 2c, d). Although none of the calculated depth profiles exactly matches the measured profile in Gold Basin samples, we can use the calculations to constrain the pre-atmospheric size of the Gold Basin meteoroid. The ^{10}Be(s) and ^{26}Al(s) concentrations in the most shielded sample of the Gold Basin shower (ZH-2) are significantly lower than the calculated production rates in the center of an object with R = 2 m, by a factor of ~2 in the Honda model and a factor of 3–4 in the LCS model. This confirms that the Gold Basin meteoroid must have had a radius significantly larger than 2 m. Because the concentrations of ^{10}Be(s) and ^{26}Al(s) in the least shielded samples (UA-1217 and UA-682) are ~10% higher than those calculated by the LCS model for a 5 m radius, we conclude that the radius of the Gold Basin meteoroid could not have been larger than ~5 m, whereas the Honda model seems to constrain the radius to less than ~3 m. It must also be noted, that for Gold Basin samples with high shielding, the ^{10}Be and ^{26}Al concentrations fall below the calculated profiles for a 5 m radius, although the Honda-model shows slightly better agreement for ^{10}Be than the LCS model. Since we do not know the pre-atmospheric depth of the samples, we cannot

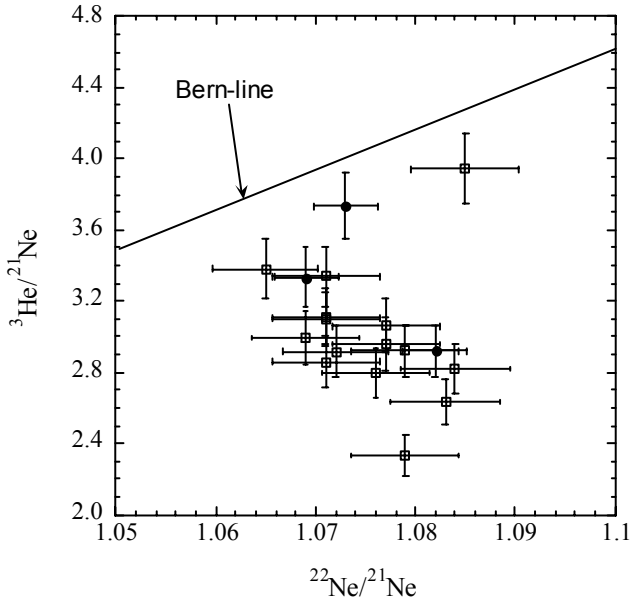

Fig. 5a. The ^{3}He/^{21}Ne versus ^{22}Ne/^{21}Ne ratio in the Gold Basin meteorite. All ^{3}He/^{21}Ne ratios are below the Bern Line (Eberhardt et al. 1966). Closed symbols represent samples with significant excess ^{21}Ne from the first-stage exposure on the parent body. Open symbols represent samples without detectable amounts of ^{21}Ne from the first stage exposure.

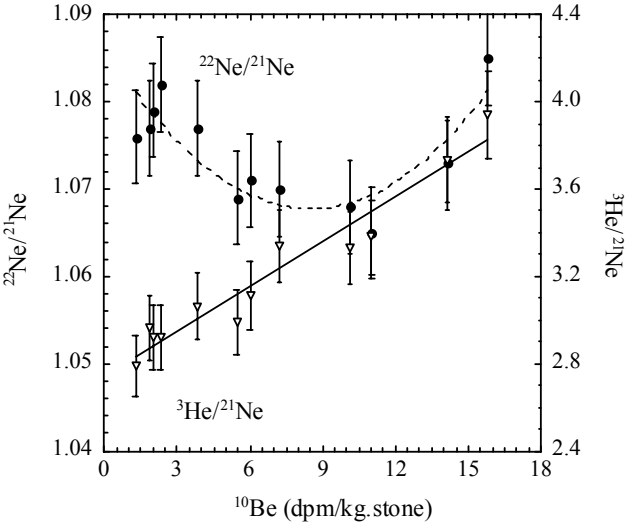

Fig. 5b. The ^{3}He/^{21}Ne and ^{22}Ne/^{21}Ne ratios in Gold Basin samples versus ^{10}Be(s), which decreases with depth. The ^{3}He/^{21}Ne continuously decreases with depth, whereas the ^{22}Ne/^{21}Ne ratio first decreases and then increases again with depth, similar to the trend predicted by Masarik, Nishiizumi, and Reedy (2001).

determine whether the calculated production rates in the stone fraction are too high or those in the metal fraction are too low, although the latter seems more likely considering the large uncertainties in the Fe(n,x)^{10}Be and Fe(n,x)^{26}Al cross sections, as discussed above. Based on the model calculations and the measured ^{10}Be and ^{26}Al concentrations, we conclude that the pre-atmospheric radius of the Gold Basin meteoroid was most likely between 2 and 5 m.

Neutron-Capture ^{36}Cl and ^{41}Ca

Concentrations of ^{36}Cl and ^{41}Ca in the stone fraction do not simply decrease from the least to the most shielded sample, but show a maximum near LPL-1012 and UA-285 (Table 2). This effect is caused by the high fluxes of thermal neutrons, which reach a maximum at depths of 50–100 cm and lead to the production of ^{36}Cl and ^{41}Ca via neutron-capture (on ^{35}Cl and ^{40}Ca). The neutron-capture contribution was determined by subtracting the spallation component from the measured concentrations of ^{36}Cl and ^{41}Ca in the stone fraction (Table 5). To estimate the production of ^{36}Cl from Ca, $P(^{36}Cl)_{Ca}$ relative to that from Fe, $P(^{36}Cl)_{Fe}$, we calculated the $P(^{36}Cl)_{Ca}/P(^{36}Cl)_{Fe}$ ratio as a function of the ^{10}Be(s)/^{10}Be(m) ratio in each sample (Welten et al. 2001b). We thus found $P(^{36}Cl)_{Ca}/P(^{36}Cl)_{Fe}$ ratios ranging from 13–24, significantly higher than the values of 8–12 derived for small to medium sized meteorites and the lunar surface (Nishiizumi et al. 1991). We estimate the relative contribution of ^{36}Cl from K at ~5% of the total spallation component, based on a constant $P(^{36}Cl)_K/P(^{36}Cl)_{Ca}$ production ratio of 1.8 (Welten et al. 2001b). We assume that all the spallation-produced ^{36}Cl in the metal fraction remained in the meteorite upon weathering of the metal, i.e. the meteorite samples behaved as a closed system.

For ^{41}Ca, the spallation contribution was derived from the concentrations of Fe, Ni, and Ca in the stone fraction and the concentration of ^{41}Ca in the metal fraction, assuming $P(^{41}Ca)_{Ni} = P(^{41}Ca)_{Fe}$ and $P(^{41}Ca)_{Ca} = 6*P(^{41}Ca)_{Fe}$ (Vogt et al. 1991). The neutron-capture component of ^{41}Ca was normalized to the amount of Ca in each sample (Table 5).

Fig. 3 shows the neutron-capture components of ^{36}Cl and ^{41}Ca as a function of the ^{10}Be concentration in the stone fraction, which decreases with depth. Neutron-capture ^{36}Cl and ^{41}Ca first increase from UA-682 to UA-285 and then decrease with depth. Neutron-capture ^{36}Cl shows more scatter than ^{41}Ca, which is probably due to variations in the indigenous Cl concentration, a quantity which is difficult to measure. From the neutron-capture ^{36}Cl and ^{41}Ca concentrations, corrected for a terrestrial age of 15 kyr, and the thermal neutron-capture cross sections for ^{35}Cl (43.6 b) and ^{40}Ca (0.44 b), we estimate that the Cl concentrations range from 100 to 200 ppm, with an average value of 140 ± 30 ppm. In Fig. 4, we compare the neutron-capture ^{41}Ca concentrations in Gold Basin with calculated depth profiles for L chondrites having radii between 1 and 5 m as well as for 2π exposure geometry. Neutron-capture ^{41}Ca depth profiles were calculated by the LCS model (Fig. 4a) as well as the semi-empirical model of Nagai et al. (1993) (Fig 4b). The production rates of ^{41}Ca in the Moon, calculated by the LCS model, are in agreement with measured values in an

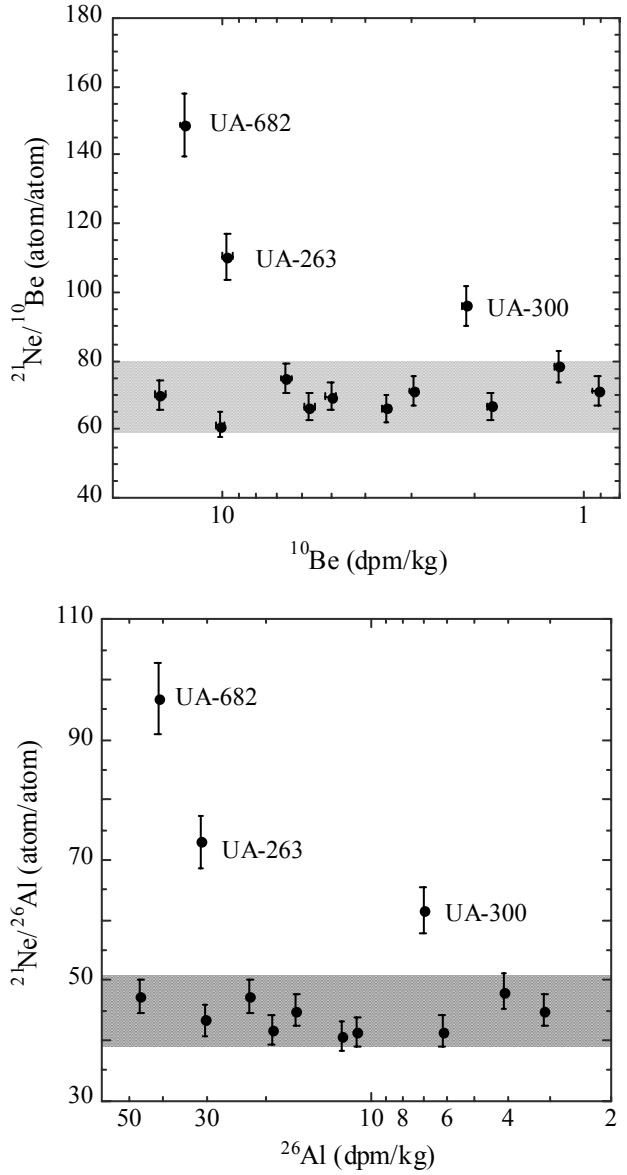

Fig. 6. The ^{21}Ne/^{10}Be (a) and ^{21}Ne/^{26}Al (b) ratios in 13 Gold Basin samples as a function of bulk ^{10}Be and ^{26}Al concentrations, which decrease with shielding depth (from left to right). The large variations in the ^{21}Ne/^{10}Be and ^{21}Ne/^{26}Al ratios do not correlate with shielding depth, but can be explained by a complex exposure history. Ten samples show relatively constant ^{21}Ne/^{10}Be and ^{21}Ne/^{26}Al ratios of 70 ± 5 and 44 ± 3 atom/atom, respectively. These ratios correspond to a second-stage exposure age of ~18 Myr. The other three samples show variable excesses of ^{21}Ne accumulated during the first-stage exposure on the surface of the L chondrite parent body.

Apollo 15 drill core, although the model slightly overestimates the production rate at depths >100 g/cm^2 (Nishiizumi et al. 1997). The model of Honda (Nagai et al. 1993) overestimates ^{41}Ca concentrations in near-surface samples, but for larger depths, the concentrations are very similar to those calculated by the LCS model. The relatively low peak value of 0.95 ± 0.07 dpm/gCa in the neutron-capture ^{41}Ca profile of Gold Basin is consistent with a radius of at least 3–5 m. The lowest value of ~0.2 dpm/gCa also requires a radius larger than ~2.5 m. As the ^{10}Be data constrain the radius to less than 5 m, we conclude that the radius of the Gold Basin meteoroid was most likely between 3 and 5 m.

Table 6. Estimated depth (in cm) of Gold Basin samples in the pre-atmospheric meteoroid, based on measured concentrations of ^{10}Be(s), ^{10}Be(m), ^{26}Al(s), and neutron-capture ^{41}Ca and calculated production rates using the LCS model for an object with a 5 m radius.

Sample	^{10}Be(s)	^{10}Be(m)	^{26}Al(s)	^{41}Ca(nc)	Average
UA-1217	<10	–	<10	6	8 ± 2
UA-682	10	14	16	7	12 ± 5
UA-263	37	30	40	(8)	36 ± 5
UA-1164	42	34	40	(15)	39 ± 5
LPL-1012	50	49	50	(20)	50 ± 5
UA-285	66	62	65	(25–75)	64 ± 5
UA-274	75	–	73	(25–75)	75 ± 5
UA-418	83	72	84	98	84 ± 11
UA-426	103	93	102	108	102 ± 6
ZH-3	112	108	107	106	109 ± 5
UA-300	130	–	131	129	130 ± 5
LPL-1011	127	125	136	142	132 ± 8
UA-639	139	130	140	131	135 ± 5
UA-1188	160	145	160	164	157 ± 8
ZH-2	172	168	174	–	171 ± 5

Values in parentheses are not included in the average.

Noble Gas Results

Concentrations of cosmogenic ^{21}Ne vary by a factor of 20, whereas cosmogenic ^{3}He varies by a factor of 30 (Table 3). The $(^3He/^{21}Ne)_c$ ratio ranges from 2.3 to 4.0, while the $(^{22}Ne/^{21}Ne)_c$ ratio is relatively constant between 1.06–1.09. The narrow range in the ^{22}Ne/^{21}Ne ratio is similar to those observed in other large objects, such as Jilin (Begemann et al. 1985, 1996) and Chico (Garrison et al. 1992), but the range in the ^{3}He/^{21}Ne ratios is much different from those in Jilin (1.2–2.4) and Chico (3.5–4.2). The relation between the two shielding parameters, ^{3}He/^{21}Ne and ^{22}Ne/^{21}Ne, is shown in Fig. 5a. Since all ^{3}He/^{21}Ne ratios in Gold Basin are below the Bern-line (Eberhardt et al. 1966), one could argue that the low ^{3}He/^{21}Ne ratios are due to diffusion losses of ^{3}He, either during irradiation (on the parent body or in space) or due to weathering effects during its terrestrial residence. Although ^{3}He losses were found for some weathered chondrite finds (Herzog and Cressy 1976; Gibson and Bogard 1978), Fig. 5b shows that the ^{3}He/^{21}Ne ratio is linearly correlated to the ^{10}Be concentration in the stone fraction, which for the Gold Basin samples, decreases with increasing shielding. Thus, the relatively low ^{3}He/^{21}Ne ratios can mainly be ascribed to extremely high shielding

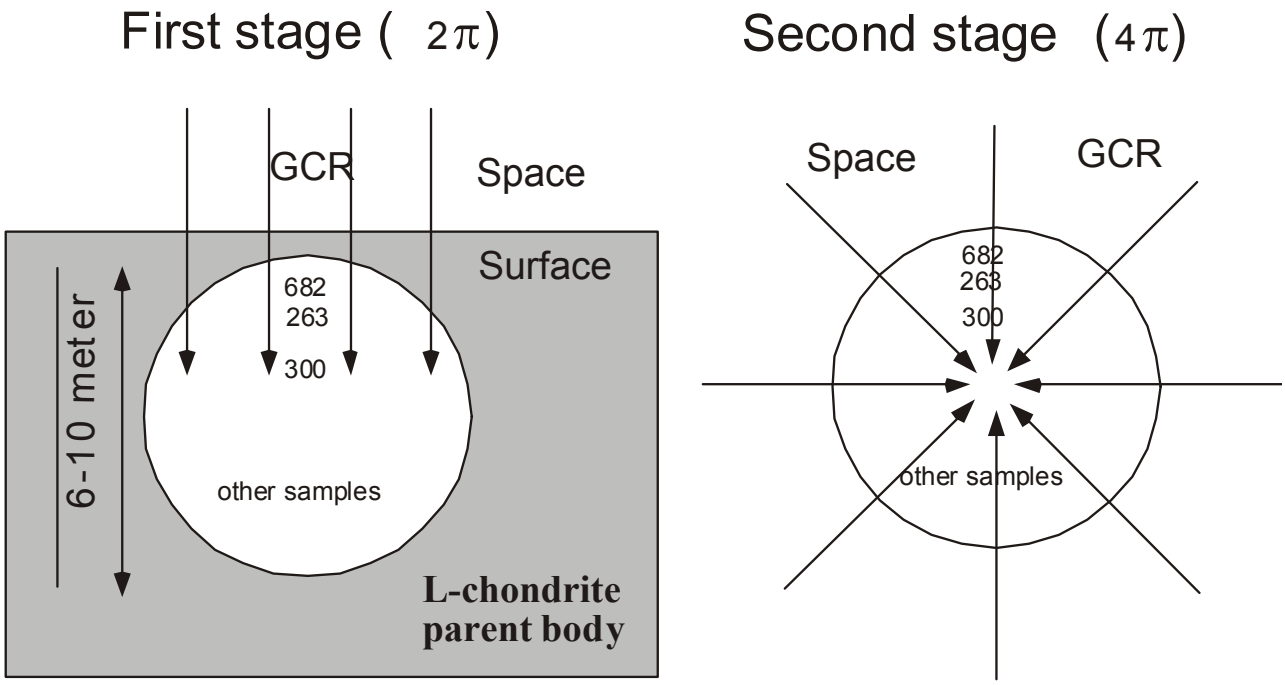

Fig. 7. A schematic drawing of the complex exposure history of the Gold Basin meteoroid. In the first stage, some of the Gold Basin samples were close enough to the surface of their parent body to be exposed to cosmic rays, while others were buried much deeper. After ejection from the parent body, a 6–10 meter large object was irradiated in space long enough to saturate all the radionuclides we measured. The relative positions of the samples was derived from the $^{21}Ne/^{10}Be$ versus ^{10}Be systematics of Fig. 6a.

conditions. At the same time, the $^{22}Ne/^{21}Ne$ ratio first decreases and then increases with increasing shielding (Fig. 5b), a trend that is different to that usually observed. Although some complications arise due to the fact that some samples contain some cosmogenic He and Ne from a previous exposure stage (see below), it is clear that the Gold Basin data confirm the model calculations by Masarik, Nishiizumi, and Reedy (2001), which predict that at very large shielding, the $^{22}Ne/^{21}Ne$ ratio increases again from a minimum value of ~1.07, while the $^{3}He/^{21}Ne$ ratio continues to decrease with depth. This shows how ambiguous the $^{22}Ne/^{21}Ne$ shielding parameter is if no independent information about the pre-atmospheric size of a meteorite is available.

Exposure History

Wieler et al. (2000) reported ^{10}Be-^{21}Ne exposure ages between 15 and 30 Myr and suggested that some samples may require a complex exposure history. Fig. 6a shows that the $^{21}Ne/^{10}Be$ ratios (atom/atom) do not show a clear trend with shielding conditions, but rather show two groups. Most samples show relatively constant ratios of 60–80, whereas three samples (UA-263, 300, and 682) show much higher ratios (95–150). Fig. 6b shows the same two "groups" for the $^{21}Ne/^{26}Al$ ratios. The possibility that our samples represent two (or more) separate showers is highly unlikely, since the ^{14}C-^{10}Be ages of samples from the two groups are identical (Kring et al. 2001). We therefore conclude that the large variations in the $^{21}Ne/^{10}Be$ and $^{21}Ne/^{26}Al$ ratios can only be explained by a complex exposure history, as shown in Fig. 7. In this scenario, the radionuclides and the noble gases from most samples were produced during the second stage exposure, whereas three samples (UA-263, 300, and 682) contain up to ~120% excess of ^{21}Ne from a previous exposure, most likely on the L chondrite parent body (or one of the L chondrite parent bodies (Haack et al. 1996). Apparently, these three samples were relatively close to the surface of the parent body, whereas other samples were buried too deep to produce detectable amounts of ^{21}Ne. This exposure condition is consistent with the large size (3–5 m radius) of the Gold Basin meteoroid. In the most recent exposure, the samples with the highest ^{21}Ne production from the first stage (UA-263 and 682) are close to the surface of the meteoroid, while the samples with the lowest (or no) ^{21}Ne from the first stage, are closer to the center or on the opposite side of the meteoroid.

The duration of the more recent exposure of Gold Basin can be determined from the group of samples with low $^{21}Ne/^{10}Be$ and $^{21}Ne/^{26}Al$ ratios. Ten samples show a relatively constant $^{21}Ne/^{10}Be$ atom ratio of 70 ± 5 (Fig. 6a) and an

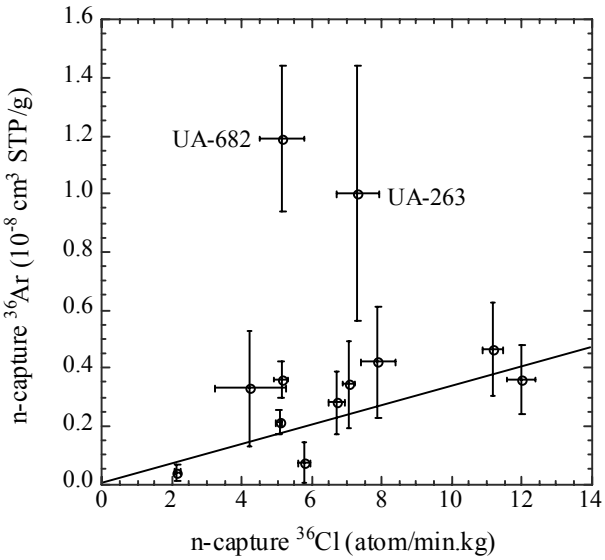

Fig. 8. Estimated concentrations of neutron-capture ^{36}Ar as a function of measured concentrations of neutron-capture ^{36}Cl. For most samples, the neutron-capture ^{36}Ar component is consistent with a single stage exposure of ~18 Myr, except for UA-682 and UA-263, which contain up to six times more neutron-capture ^{36}Ar than expected on the basis of a simple exposure history. The higher ^{36}Ar excess in UA-682 suggests that during the first-stage irradiation, this sample was at least 30 cm further from the surface than during the second stage 4π irradiation.

average ^{21}Ne/^{26}Al atom ratio of 44 ± 3 (Fig. 6b). The P(^{10}Be)/P(^{21}Ne) production rate ratio is not well known for extremely large objects: 1) the semi-empirical model of Graf, Baur, and Signer (1990a) suggests a relatively constant production rate ratio of ~0.14, 2) the model used here shows ratios decreasing from 0.14 to 0.12 with increasing size and depth, and 3) the work of Leya et al. (2000) suggests that the P(^{10}Be)/P(^{21}Ne) production ratio might be as low as 0.10 for high shielding conditions. The calculated ^{21}Ne/^{10}Be age ranges from 21 Myr using Graf's model, 18–21 Myr using this work, and as low as 15 Myr using the ratio of Leya et al. (2000). The lower estimate coincides with a peak at ~15 Myr in the exposure age distribution of L chondrites with low ^{40}Ar contents (Marti and Graf 1992), to which Gold Basin belongs. However, calculations in this work using LCS show that the P(^{26}Al)/P(^{21}Ne) production rate ratio in large chondritic objects is relatively independent of size and depth, showing an average value of 0.41, and should therefore give a more reliable age. For eight samples with no detectable excess ^{21}Ne from the first stage, i.e., those with ^{21}Ne/^{26}Al ratios in a narrow range of 44 ± 3 (Fig. 6b), we determine a second-stage exposure age of 18 ± 2 Myr. The error is mainly due to an estimated 10% uncertainty in the P(^{26}Al)/P(^{21}Ne) ratio. This exposure age corresponds to a P(^{10}Be)/P(^{21}Ne) production rate ratio of ~0.12, which is consistent with the LCS model calculations for depths >80 cm in objects with a radius larger than 3 m.

Sample Depth

The depth (D) of each sample in the pre-atmospheric object can be estimated from the measured concentrations of ^{10}Be(s), ^{10}Be(m), ^{26}Al(s), ^{26}Al(m), and neutron-capture ^{41}Ca. We did not use the ^{26}Al concentration in the metal fraction, since the LCS model does not yield reliable results for this spallation product from Fe and Ni, as discussed previously. The depth estimates from the other four parameters, using the LCS model, are generally consistent if we assume a pre-atmospheric radius of 5 m (Table 6). However, for depths below 70 cm, the neutron-capture ^{41}Ca concentration generally gives much lower depth estimates (by up to ~30 cm) than the ^{10}Be and ^{26}Al concentrations. In principle, this discrepancy could be explained by a recent collision on the Gold Basin meteoroid, less than ~0.5 Myr ago, removing a chunk of ~30 cm diameter from the surface of the meteoroid. In such a scenario, the ^{41}Ca concentrations would adjust to the new size and shape of the meteoroid, whereas the ^{10}Be and ^{26}Al concentrations would mainly reflect the previous size and shape, corresponding to greater depths. However, it is also possible that the observed differences between the estimated sample depths are simply due to uncertainties of ~10% in the absolute production rates calculated with the LCS model. We thus conclude that the general agreement between the four depth estimates is acceptable considering the uncertainties involved.

Neutron-Capture ^{36}Cl and ^{36}Ar

The neutron capture component of ^{36}Ar (from decay of neutron-capture-produced ^{36}Cl) is difficult to determine, because the measured ^{36}Ar concentration is a mixture of spallation (sp), neutron-capture (nc), and trapped (tr) Ar. As the ^{36}Ar/^{38}Ar ratio of the trapped component is ~8 times higher than that of the spallogenic component, the measured ^{36}Ar/^{38}Ar ratio is generally used to correct for trapped Ar. For meteorites with a neutron-capture ^{36}Ar component, this method leads to an overcorrection for trapped Ar, resulting in too low cosmogenic ^{38}Ar concentrations (Bogard et al. 1995). This becomes evident when we evaluate the nominal cosmogenic ^{21}Ne/^{38}Ar ratio, which is relatively constant at 7–9 in medium-sized meteorites such as Knyahinya (Graf et al. 1990b), but shows values of 7–43 for the Gold Basin samples. By assuming that the true cosmogenic ^{21}Ne/^{38}Ar ratio in Gold Basin is 8 ± 1 we can estimate the amount of neutron-capture ^{36}Ar in each sample, using the following equation:

$$^{36}Ar_{n\text{-}cap} = {}^{36}Ar_{meas} - 0.65*(^{21}Ne_{cos}/8) - 5.32*(^{38}Ar_{meas} - {}^{21}Ne_{cos}/8) \quad (1)$$

The estimated concentrations of neutron-capture ^{36}Ar are listed in Table 5. The quoted uncertainties include the uncertainty in the adopted value of 8 ± 1 for the cosmogenic ^{21}Ne/^{38}Ar ratio. This ratio is not well known for large

meteorites such as Gold Basin, but seems to give consistent results as shown in Fig. 8.

Fig. 8 shows that, for most Gold Basin samples, the estimated amount of neutron-capture ^{36}Ar is consistent with a single exposure history of ~18 Myr, but that the two samples with the largest ^{21}Ne excesses (UA-682 and 263) also show excess ^{36}Ar from the first-stage exposure. The excess of neutron-capture ^{36}Ar is more or less independent evidence for large contributions from a first stage and is consistent with our conclusion of a complex exposure history. UA-682 contains a higher excess neutron-capture ^{36}Ar than UA-263 (1.01 versus 0.75 × 10^{-8} cm^3 STP/g), indicating that UA-682 experienced a higher thermal neutron flux during the first stage than UA-263. This is opposite to the observation from neutron-capture-produced ^{36}Cl in the most recent exposure and can only be explained by considerable shielding of the Gold Basin meteoroid on the parent body, i.e. by shifting the samples to greater depths in the neutron-capture depth profile. A shift of ~40 cm due to burial on the parent body brings UA-682 close to the peak in the thermal neutron depth profile, whereas UA-263 was buried deeper and thus experienced a lower thermal neutron flux. From the neutron-capture ^{36}Ar and ^{36}Cl data alone we can thus only constrain the burial depth to >40 cm.

Since the depth profiles of spallation-produced ^{21}Ne and neutron-capture-produced ^{36}Ar are quite different (Fig. 9), we will estimate the burial depths of UA-682 and UA-263 in the first stage from the observed excesses of ^{21}Ne and neutron-capture ^{36}Ar. From Fig. 6, we can determine the excess of ^{21}Ne from the first stage at 4.3 and 1.7 × 10^{-8} cm^3 STP/g in UA-682 and UA-263, respectively. This gives ^{21}Ne(sp)/^{36}Ar(nc) ratios of 4.3 ± 1.1 and 2.2 ± 1.3 for the first stage exposure of UA-682 and UA-263, respectively. The uncertainty in the ratio for UA-263 is rather large, mainly because the three aliquots measured give a wide range in neutron-capture ^{36}Ar, ranging from 0.5–1.3 × 10^{-8} cm^3 STP/g, possibly due to the inhomogeneous distribution of Cl. For this sample, we can therefore only estimate a lower limit of ~50 cm for the burial depth. However, the ratio for UA-682 corresponds to a burial depth of ~60 cm, with lower and upper limits of 40 and 120 cm, respectively. The corresponding ^{21}Ne production rates, which can be derived from Fig. 9, yield a ^{21}Ne exposure age of 50 Myr, with lower and upper limits of 35 and 150 Myr.

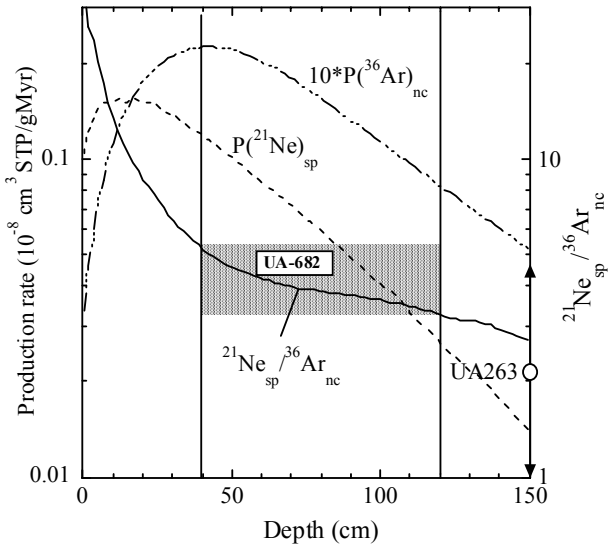

Fig. 9. The excess of spallation-produced ^{21}Ne and neutron-capture-produced ^{36}Ar in UA-682 and UA-263 compared to calculated production rates for 2π exposure geometry. The ^{21}Ne production rates are from Leya et al. (2001). The neutron-capture ^{36}Ar production rate is based on an indigenous Cl content of 140 ppm, which leads to a peak value of 11.5 dpm/kg in the neutron-capture ^{36}Cl profile, i.e., similar to the maximum value observed in Gold Basin (Fig. 2). The ^{21}Ne(sp)/^{36}Ar(nc) ratio in UA-682 corresponds to a burial depth of ~60 cm, with lower and upper limits of 40 and 120 cm. The estimated burial depth of 60 cm corresponds to a ^{21}Ne exposure age of 50 Myr, with lower and upper limits of 35 and 150 Myr.

Thermal History

The measured ^{4}He concentrations range from 90–280 × 10^{-8} cm^3 STP/g and show a linear increase with cosmogenic ^{3}He concentrations, which range from 0.8–30 × 10^{-8} cm^3 STP/g (Fig. 10a). The slope of this correlation yields a cosmogenic ^{4}He/^{3}He ratio of 6.2 ± 0.2, consistent with the value of 6.1 ± 0.3 found by Alexeev (1998), whereas the intercept at ^{3}He$_c$ = 0 yields an average radiogenic ^{4}He concentration of 102 ± 10 × 10^{-8} cm^3 STP/g. This low concentration corresponds to a U, Th-He gas retention age of 360 ± 40 Myr, which coincides with the major L chondrite peak of 340 ± 50 Myr (Alexeev, 1998). The measured ^{40}Ar concentration varies from 120–1200 × 10^{-8} cm^3 STP/g. However, most of the high values (>300 × 10^{-8} cm^3 STP/g) correspond to Gold Basin samples with a large contribution of trapped Ar. A plot of measured ^{40}Ar versus trapped ^{36}Ar (^{36}Ar$_{tr}$ = ^{36}Ar$_m$ – ^{36}Ar$_{sp}$ – ^{36}Ar$_{nc}$) shows a fairly good correlation (R = 0.98) for 26 out of the 32 samples (Fig. 10b). Extrapolation to ^{36}Ar$_{tr}$ = 0 yields an average radiogenic ^{40}Ar concentration of 140 ± 40 × 10^{-8} cm^3 STP/g, which corresponds to a K-Ar age of 400 ± 100 Myr. This age is consistent with the U, Th-He age and coincides with the main peak in the L chondrite K-Ar age distribution (Heymann 1967). The low ^{4}He-U/Th and K-Ar ages indicate that the Gold Basin parent body experienced a recent major impact event 300–400 Myr ago. Contrary to the radiogenic ^{4}He and ^{40}Ar concentrations in Jilin (Begemann et al. 1985, 1996), those in Gold Basin do not show any correlation with pre-atmospheric depth. This lack of correlation suggests that the radiogenic gas loss did not occur during or after ejection of the Gold Basin meteoroid from its parent body. This is confirmed by the cosmogenic ^{3}He concentrations, which do not show significant losses in those Gold Basin samples that experienced a first stage exposure near the surface of the parent body. Based on the first stage exposure of 35–150 Myr,

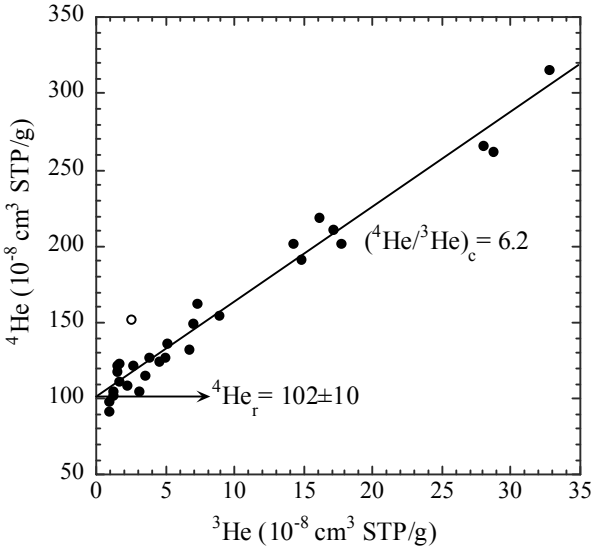

Fig. 10a. The measured ^{4}He concentration in Gold Basin shows a linear increase as a function of the meaured (cosmogenic) ^{3}He concentration in 31 (represented by closed symbols) of the 32 analyzed samples. The correlation shows a slope of 6.2 ± 0.2, which represents the cosmogenic ^{4}He/^{3}He ratio, whereas the intercept at ^{3}He = 0 represents the radiogenic ^{4}He component of 102 ± 10 × 10^{-8} cm^3 STP/g.

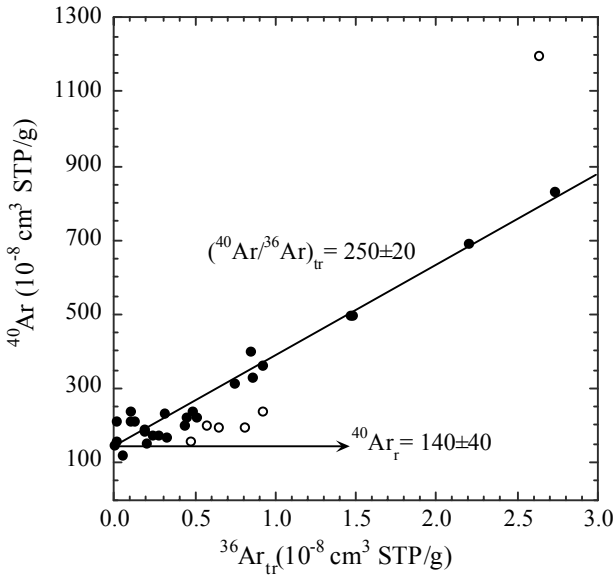

Fig. 10b. The measured ^{40}Ar concentration in Gold Basin shows a linear increase as a function of the trapped (measured–spallogenic–neutron-capture) ^{36}Ar component in 26 (represented by closed symbols) of the 32 analyzed samples. The correlation shows a slope of 250 ± 20, which represents the ^{40}Ar/^{36}Ar ratio of the trapped component, whereas the intercept at ^{36}Ar$_{tr}$ = 0 represents the radiogenic ^{40}Ar component of 140 ± 40 × 10^{-8} cm^3 STP/g.

it is unlikely that the major impact event that outgassed many L chondrites ~350 Myr ago (Alexeev 1998) and possibly disrupted the L chondrite parent body (Haack et al. 1996), brought the Gold Basin meteoroid close enough to the surface of its parent body to become exposed to cosmic rays.

We conclude that the Gold Basin meteorite shows evidence of least three different impacts: 1) a major impact event 300–400 Myr ago, which resulted in the loss of radiogenic ^{4}He and ^{40}Ar in Gold Basin and many other L chondrites, 2) one (or several) impacts ~50–170 Myr ago, which brought Gold Basin close enough to the surface of its parent body to become exposed to cosmic rays, and 3) an impact ~18 Myr ago, which blasted the Gold Basin meteoroid off its parent body.

CONCLUSIONS

The concentrations of cosmogenic ^{10}Be, ^{26}Al, ^{36}Cl, and ^{41}Ca in the metal and stone fraction of ten Gold Basin fragments combined with cosmogenic noble gases are consistent with a simple exposure history of 18 Myr in a large object. Based on Monte Carlo calculations using the LAHET Code System, the measured concentrations correspond to shielding depths of ~10 cm to 150–200 cm in an object with a pre-atmospheric radius of 3–5 m. However, cosmogenic nuclide concentrations in three fragments require a complex exposure history with a first stage irradiation of 35–150 Myr near the surface of its parent body and a second stage of ~18 Myr as an object of 3–5 m in radius. The duration of the second stage is the longest reported for any stony meteorite with a complex exposure history (Nishiizumi et al. 1979; Vogt et al. 1993; Wieler et al. 1996; Herzog et al. 1997; Welten et al. 2001b; Ferko et al. 2000). From those samples which show no significant contribution of ^{21}Ne from the first stage exposure, we conclude that the ^{10}Be/^{21}Ne and ^{26}Al/^{21}Ne ratios do not show any systematic variation with depth, but remain constant, within experimental errors, throughout the meteorite.

The cosmogenic ^{3}He/^{21}Ne versus ^{22}Ne/^{21}Ne ratios of Gold Basin do not follow the Bern-line. Instead, the ^{22}Ne/^{21}Ne ratio increases with increasing shielding depth (over ~1 m), which is predicted by LCS model calculations. On the other hand, it seems that ^{10}Be and ^{26}Al production rates in the metal fraction of large objects are underestimated by the LCS model, as well as by the Honda model.

From the noble gases and radionuclides, we can reconstruct the location of the samples during the first (2π) and second (4π) exposure stages. We did not find a correlation with the location of find in the field, because our samples were selected early in the Gold Basin discovery process and only represent a small fraction of what is now known as the total Gold Basin strewn field (D. Kring, pers. comm.).

The low radiogenic ^{4}He and ^{40}Ar concentrations in Gold Basin indicate a major outgassing event between 300 and 400 Myr ago, which coincides with the main impact event on the L chondrite parent body. Cosmic ray exposure of the Gold Basin meteoroid on the parent body must have started after this main impact, since no cosmogenic ^{3}He was lost.

Acknowledgments–We thank D. Kring for selecting and providing the Gold Basin samples. This work was supported by NASA grant NAG5-4992, the Swiss National Science Foundation, and was performed under the auspices of the U.S. DOE by the University of California, LLNL under contract No. W-7405-ENG-48. We are grateful to John Southon and Bob Finkel for assistance with the AMS measurements and to Ludolf Schultz and Greg Herzog for critical reviews.

REFERENCES

Albrecht A., Schnabel C., Vogt S., Xue S., Herzog G. F., Begemann F., Weber H. W., Middleton R., Fink D., and Klein J. 2000. Light noble gases and cosmogenic radionuclides in Estherville, Budulan, and other mesosiderites: Implications for exposure histories and production rates. *Meteoritics & Planetary Science* 35:975–986.

Alexeev V. A. 1998. Parent bodies of L and H chondrites: Times of catastrophic events. *Meteoritics & Planetary Science* 33:145–152.

Begemann F., Li Z., Schmitt-Strecker S., Weber H. W., and Xu Z.. 1985. Noble gases and the history of Jilin meteorite. *Earth and Planetary Science Letters* 72:247–262.

Begemann F., Caiyun F., Weber H. W., and Xianbin W. 1996. Light noble gases in Jilin: More of the same and something new. *Meteoritics & Planetary Science* 31:667–674.

Bhandari N. et al. 1993. Depth and size dpendence of cosmogenic nuclide production rates in stony meteoroids. *Geochimica et Cosmochimica Acta* 57:2361–2375.

Bland P. A., Sexton A. S., Jull A. J. T., Bevan A. W. R., Berry F. J., Thornley D. M., Astin T. R., Britt D. T., and Pillinger C. T. 1998. Climate and rock weathering: A study of terrestrial age dated ordinary chondritic meteorites from hot desert regions. *Geochimica et Cosmochimica Acta* 62:3169–3184.

Bogard D. D., Nyquist L. E., Bansal B. M., Garrison D. H., Wiesmann H., Herzog G. F., Albrecht A. A., Vogt S., and Klein J. 1995. Neutron-capture ^{36}Cl, ^{41}Ca, ^{36}Ar and ^{150}Sm in large chondrites: Evidence for high fluences of thermalized neutrons. *Journal of Geophysical Research* 100:E9401–E9416.

Briesmeister J. F. 1993. MCNP—A general Monte Carlo N-Particle transport code, Version 4A. Los Alamos National Laboratory Report LA-12625-M:693.

Davis J. C. et al. 1990. LLNL/UC AMS facility and research program. *Nuclear Instruments & Methods* B52:269–272.

Dittrich B., Herpers U., Hofmann H. J., Wölfli W., Bodemann, Lüpke M., Michel R., Dragovitch, and Filges D. 1990. AMS measurments of thin-target cross sections for the production of ^{10}Be and ^{26}Al by high-energy protons. *Nuclear Instruments & Methods* B52:588–594.

Eberhardt P., Eugster O., Geiss J., and Marti K. 1966. Rare gas measurements in 30 stone meteorites. *Zeitschrift für Naturforschung* 21a:414–426.

Ferko T. E., Schultz L., Franke L., Bogard D. D., Garrison D. H., Hutchinson R., and Lipschutz M. E. 2000. Exposure history of the Mocs (L6) chondrite: a study of strewn field samples. *Meteoritics & Planetary Science* 35:1215–1227.

Ferko T. E. et al. 2002. The irradiation history of the Ghubara (L5) regolith breccia. *Meteoritics & Planetary Science* 37:311–328.

Garrison D. H., Bogard D. D., Albrecht A. A., Vogt S., Herzog G. F., Klein J., Fink D., Dezfouly-Arjomandy B., and Middleton R. 1992. Cosmogenic nuclides in core samples of the Chico L6 chondrite: Evidence for irradiation under high shielding *Meteoritics* 27:371–381.

Gibson E. K. and Bogard D. D. 1976. Chemical alterations of the Holbrook chondrite resulting from terrestrial weathering. *Meteoritics* 13:277–289.

Graf T., Baur H., and Signer P. 1990a. A model for the production of cosmogenic nuclides in chondrites. *Geochimica et Cosmochimica Acta* 54:2521–2534.

Graf T., et al. 1990b. Cosmogenic nuclides and nuclear tracks in the chondrite Knyahinya. *Geochimica et Cosmochimica Acta* 54: 2511–2520.

Haack H., Farinella P., Scott E. R. D., and Keil K. 1996. Meteoritic, asteroidal, and theoretical constraints on the 500 Ma disruption of the L chondrite parent body. *Icarus* 119:182–191.

Herzog G. F. and Cressy P. J. 1976. ^{26}Al losses from weathered chondrites. *Meteoritics* 11:59–68.

Herzog G. F., Vogt S., Albrecht A., Xue S., Fink D., Klein J., Middleton R., Weber H. W., and Schultz L. 1997. Complex exposure histories for meteorites with "short" exposure ages. *Meteoritics & Planetary Science* 32:413–422.

Heymann D. 1967. On the origin of hypersthene chondrites: Ages and shock effects of black chondrites. *Icarus* 6:189–221.

Heymann D., Lipschutz M. E., Nielsen B., and Anders E. 1966. Canyon Diablo meteorite: Metallographic and mass spectrometric study of 56 fragments. *Journal of Geophysical Research* 71:619–641.

Honda M. 1988. Statistical estimation of the production of cosmic-ray-induced nuclides in meteorites. *Meteoritics* 23:3–12.

Honda M., Caffee M. W., Miura Y. N., Nagai H., Nagao K., and Nishiizumi K. 2002. Cosmogenic nuclides in the Brenham Pallasite. *Meteoritics & Planetary Science* 37:1711–1728.

Imamura M., Nagai H., Takabatake M., Shibata S., Kobayashi K., Yoshida K., Ohashi H., Uwamino Y., and Nakamura T. 1990. Measurements of production cross sections of ^{14}C and ^{26}Al with high-energy neutrons up to En = 38 MeV by accelerator mass spectrometry. *Nuclear Instruments & Methods* B52:595–600.

Jarosewich E. 1990. Chemical analyses of meteorites: A compilation of stony and iron meteorites. *Meteoritics* 25:323–337.

Kring D. A., Jull A. J. T., McHargue L. R., Bland P. A., Hill D. H., and Berry F. J. 2001. Gold Basin meteorite strewn field, Mojave Desert: Relict of a small Late Pleistocene impact event. *Meteoritics & Planetary Science* 36:1057–1066.

Lavielle B., Marti K., Jeannot J. P., Nishiizumi, and Caffee M. 1999. The ^{36}Cl-^{36}Ar-^{40}K-^{41}K records and cosmic-ray production rates in iron meteorites. *Earth and Planetary Science Letters* 170:93–104.

Leya I. and Michel R. 1998. Modeling the cosmic-ray record of the iron meteoroid Grant (abstract #1172). 29th Lunar and Planetary Science Conference. CD-ROM.

Leya I., Lange H. -J., Neumann S., Wieler R., and Michel R. 2000. The production of cosmogenic nuclides in stony meteoroids by galactic cosmic ray particles. *Meteoritics & Planetary Science* 35:259–286.

Leya I., Neumann S., Wieler R., and Michel R. 2001. The production of cosmogenic nuclides by galactic cosmic ray particles for 2π exposure geometries. *Meteoritics & Planetary Science* 36:1547–1561.

Marti K. and Graf Th. 1992. Cosmic-ray exposure history of ordinary chondrites. *Annual Review of Earth and Planetary Sciences* 20: 221–243.

Masarik J. and Reedy R. C. 1994a. Effects of bulk composition on nuclide production processes in meteorites. *Geochimica et Cosmochimica Acta* 58:5307–5317.

Masarik J. and Reedy R. C. 1994b. Effects of meteoroid shape on cosmogenic nuclide production rates (abstract). 25th Lunar and Planetary Science Conference. pp. 843–844.

Masarik J., Nishiizumi K., and Reedy R. C. 2001. Production rates of cosmogenic helium-3, neon-21 and neon-22 in ordinary

chondrites and the lunar surface. *Meteoritics & Planetary Science* 36:643–650.

Merchel S., Faestermann T., Herpers U., Knie K., Korschinek G., Leya I., Lipshutz M. E., and Michel R. 2001. Cosmogenic nuclides in iron meteorites: Challenging Canyon Diablo (abstract). *Meteoritics & Planetary Science* 36:A132.

Michlovich E. S., Vogt S., Masarik J., Reedy R. C., Elmore D., and Lipschutz M. E. 1994. ^{26}Al, ^{10}Be, and ^{36}Cl depth profiles in the Canyon Diablo iron meteorite. *Journal of Geophysical Research* 99:23, 187–23, 194.

Nagai H., Honda M., Imamura M., and Kobayashi K. 1993. Cosmogenic ^{10}Be and ^{26}Al in metal, carbon, and silicate of meteorites. *Geochimica et Cosmochimica Acta* 57:3705–3723.

Nishiizumi K., Elmore D., Ma X. Z., and Arnold J. R. 1984. ^{10}Be and ^{26}Al depth profiles in an Apollo 15 drill core. *Earth and Planetary Science Letters* 70:157–163.

Nishiizumi K., Arnold J. R., Sharma P., Kubik P. W., and Reedy R. C. 1991. Cosmogenic ^{36}Cl production on the lunar surface (abstract). 22nd Lunar and Planetary Science Conference. pp. 979–980.

Nishiizumi K., Fink D., Klein J., Middleton R., Masarik J., Reedy R. C., and Arnold J. R. 1997. Depth profile of ^{41}Ca in an Apollo 15 drill core and the low-energy neutron flux in the Moon. *Earth and Planetary Science Letters* 148:545–552.

Nishiizumi K., Caffee M. W., and Depaolo D. J. 2000. Preparation of ^{41}Ca AMS standards. *Nuclear Instruments & Methods* B172: 399–403.

Prael R. E. and Lichtenstein H. 1989. User guide to LCS: The LAHET Code System, *Los Alamos National Laboratory report* LA-UR-89-3014:76.

Rambaldi E. R., Cendales M., and Thacker R. 1978. Trace element distribution between magnetic and non-magnetic portions of ordinary chondrites. *Earth and Planetary Science Letters* 40: 175–186.

Reedy R. C., Masarik J., Nishiizumi K., Arnold J. R., Finkel R. C., Caffee M. W., Southon J., Jull A. J. T., and Donahue D. J. 1993. Cosmogenic radionuclide profiles in Knyahinya: New measurements and models (abstract). 24th Lunar and Planetary Science Conference. pp. 1195–1196.

Reedy R. C. and Masarik J. 1994. Cosmogenic nuclide depth profile in the lunar surface (abstract). 25th Lunar and Planetary Science Conference. pp. 1119–1120.

Sharma P., Kubik P. W., Fehn U., Gove G. E., Nishiizumi K., and Elmore D. 1990. Development of ^{36}Cl standards for AMS. *Nuclear Instruments & Methods* B52:410–415.

Vogt S., Fink D., Klein J., Middleton R., Dockhorn B., Korschinek G., Nolte E., and Herzog G. F. 1991. Exposure histories of the lunar meteorites: MAC 88104, MAC 88105, Y791197, and Y86032. *Geochimica et Cosmochimica Acta* 55:3157–3166.

Vogt S. et al. 1993. On the Bur Gheluai H5 chondrite and other meteorites with complex exposure histories. *Meteoritics* 28:71–85.

Welten K. C. 1999. Concentrations of siderophile elements in nonmagnetic fractions of Antarctic H- and L-chondrites: A quantitative approach to weathering effects. *Meteoritics & Planetary Science* 34:259–270.

Welten K. C., Nishiizumi K., Caffee M. W., Schäfer J., and Wieler R. 1999. Terrestrial ages and exposure ages of Antarctic H-chondrites from Frontier Mountain, North Victoria Land. *Antarctic Meteorite Research* 12:94–107.

Welten K. C., Nishiizumi K., Caffee M. W., Masarik J., and Wieler R. 2001a. A complex exposure history of the Gold Basin L4-chondrite shower from cosmogenic radionuclides and noble gases (abstract #2110). 32nd Lunar and Planetary Science Conference. CD-ROM.

Welten K. C., Masarik J., Nishiizumi K., Caffee M. W., Klandrud S. E., Jull A. J. T., and Wieler R. 2001b. Cosmic-ray exposure history of two Frontier Mountain H-chondrite showers from the spallation and neutron-capture products. *Meteoritics & Planetary Science* 36:300–316.

Wieler R., Graf T., Pedroni A., Signer P., Pellas P., Fieni C., Suter M., Vogt S., Clayton R. N., and Laul J. C. 1989. Exposure history of the regolithic chondrite Fayetteville: II. Solar-gas-free light inclusions. *Geochimica et Cosmochimica Acta* 53:1449–1459.

Wieler R. et al. 1996. Exposure history of the Torino meteorite. *Meteoritics & Planetary Science* 31:265–272.

Wieler R., Baur H., Jull A. J. T., Klandrud S. E., Kring D. A., Leya I., and McHargue L. R. 2000. Cosmogenic helium, neon, and argon in the large Gold Basin chondrite (abstract). *Meteoritics & Planetary Science* 35:A169–170.

APPENDIX

Table A1. Noble gas concentrations (in 10^{-8} cm^3 STP/g) in Gold Basin L4 chondrite samples. Results in italics are not included in the average values, either due to possible losses of He and Ne or due to contamination with atmospheric Ar.

Sample	Mass	^{3}He	^{4}He	^{20}Ne	^{21}Ne	^{22}Ne	^{3}He/^{21}Nec	^{22}Ne/^{21}Nec	^{36}Ar	^{38}Ar	^{40}Ar	^{38}Arcos
UA-263	184.2	16.1	220	4.15	4.65	4.97	3.47	1.069	2.93	0.815	199	0.30
	178.8	14.7	192	3.99	4.48	4.80	3.28	1.070	1.40	0.662	214	0.45
	155.7	14.2	202	3.99	4.38	4.69	3.24	1.068	2.26	0.683	236	0.29
	Avg.	**15.0**	**205**	**4.04**	**4.50**	**4.82**	**3.33**	**1.069**	**2.20**	**0.72**	**216**	**0.35**
UA-274	218.2	*3.58*	*97*	*1.25*	*1.38*	*1.48*	*2.59*	*1.073*	0.88	0.270	225	0.119
	223.1	5.04	137	1.47	1.62	1.73	3.12	1.069	1.32	0.363	330	0.131
	Avg.	**5.04**	**137**	**1.47**	**1.62**	**1.73**	**3.12**	**1.069**	**1.10**	**0.317**	**278**	**0.125**
UA-285	177.6	6.86	150	1.81	2.02	2.16	3.39	1.068	1.06	0.347	226	0.166
	120.6	7.17	163	1.96	2.18	2.35	3.28	1.074	0.79	0.289	216	0.161
	Avg.	**7.01**	**157**	**1.89**	**2.10**	**2.25**	**3.33**	**1.071**	**0.93**	**0.318**	**221**	**0.164**
UA-300	206.7	2.55	123	0.77	0.84	0.91	3.02	1.080	0.60	0.166	171	0.061
	137.2	2.48	152	0.88	0.88	0.96	2.82	1.083	*1.47*	*0.283*	*366*	*0.009*
	Avg.	**2.51**	**137**	**0.83**	**0.86**	**0.94**	**2.92**	**1.082**	**0.60**	**0.17**	**171**	**0.061**
UA-418	165.5	3.58	*101*	*1.17*	*1.27*	*1.36*	*2.82*	*1.067*	1.02	0.297	316	0.118
	145.5	4.43	125	1.48	1.48	1.60	3.00	1.071	1.21	0.343	400	0.130
	Avg.	**4.43**	**125**	**1.48**	**1.48**	**1.60**	**3.00**	**1.071**	**1.12**	**0.320**	**358**	**0.124**
UA-639	252.8	1.49	112	0.45	0.49	0.54	3.02	1.082	0.72	0.15	162	0.012
	196.1	1.50	124	0.55	0.53	0.58	2.82	1.075	*3.09*	*0.58*	*835*	*–0.004*
	Avg.	**1.49**	**118**	**0.50**	**0.51**	**0.56**	**2.92**	**1.079**	**0.72**	**0.15**	**162**	**0.012**
UA-682	228.1	28.7	263	6.99	7.72	8.25	3.73	1.068	*4.81*	*1.46*	*1201*	0.63
	160.5	32.7	316	7.43	8.24	8.89	3.97	1.078	2.25	0.95	240	0.60
	153.6	28.0	267	7.20	7.98	8.57	3.51	1.073	1.47	0.86	190	0.67
	Avg.	**29.8**	**282**	**7.21**	**7.98**	**8.57**	**3.73**	**1.073**	**1.86**	**0.90**	**215**	**0.63**
UA-1164	165.9	6.55	*109*	*2.12*	*2.34*	*2.50*	*2.80*	*1.068*	0.90	0.376	174	0.24
	232.0	8.82	155	2.39	2.61	2.78	3.38	1.062	*1.79*	*0.604*	*498*	*0.30*
	Avg.	**8.82**	**155**	**2.39**	**2.61**	**2.78**	**3.38**	**1.065**	**0.90**	**0.38**	**174**	**0.24**
UA-1187	136.8	1.42	122	0.44	0.46	0.50	3.08	1.076	0.80	0.177	197	0.030
	185.2	1.43	118	0.48	0.50	0.54	2.88	1.078	*2.40*	*0.475*	*694*	*0.027*
	Avg.	**1.42**	**120**	**0.46**	**0.48**	**0.52**	**2.98**	**1.077**	**0.80**	**0.18**	**197**	**0.030**
UA-1188	128.0	1.05	103	0.341	0.366	0.395	2.88	1.078	0.94	0.225	238	0.055
	154.1	1.12	105	0.414	0.417	0.452	2.69	1.073	*1.62*	*0.330*	*498*	*0.028*
	Avg.	**1.09**	**104**	**0.38**	**0.39**	**0.42**	**2.78**	**1.076**	**0.94**	**0.23**	**238**	**0.055**
UA-1217	140.8	17.0	212	3.97	4.37	4.75	3.90	1.087	1.21	0.58	186	0.41
	124.5	17.6	203	4.04	4.42	4.79	3.99	1.083	0.85	0.54	159	0.43
	Avg.	**17.3**	**208**	**4.00**	**4.39**	**4.77**	**3.95**	**1.085**	**1.03**	**0.56**	**173**	**0.42**
UA-1221	245.9	3.41	116	1.03	1.12	1.20	3.04	1.069	0.65	0.220	204	0.110
	231.1	3.66	128	1.08	1.16	1.25	3.14	1.072	0.95	0.236	242	0.064
	Avg.	**3.53**	**122**	**1.06**	**1.14**	**1.23**	**3.09**	**1.071**	**0.80**	**0.228**	**223**	**0.087**